Elastic reflection based waveform inversion with a nonlinear approach

GEOPHYSICS®

Elastic reflection based waveform inversion with a nonlinear approach

Journal:	*Geophysics*
Manuscript ID	GEO-2016-0407.R3
Manuscript Type:	Technical Paper
Date Submitted by the Author:	12-Jul-2017
Complete List of Authors:	Guo, Qiang; King Abdullah University of Science and Technology, PSE Alkhalifah, Tariq; Astronomy and Geophysical Research Institute, KACST
Keywords:	elastic, reflection, full-waveform inversion, nonlinear
Area of Expertise:	Seismic Migration, Seismic Inversion
Note: The following files were submitted by the author for peer review, but cannot be converted to PDF. You must view these files (e.g. movies) online.	
Table.tex	

Elastic reflection based waveform inversion with a nonlinear approach

Qiang Guo* **and Tariq Alkhalifah***

**King Abdullah University of Science & Technology,*

4700 KAUST, Thuwal,

Jeddah, 23955-6900, KSA

Email: qiang.guo@kaust.edu.sa ; tariq.alkhalifah@kaust.edu.sa

(August 15, 2017)

GEO-2016-0407.R3

Running head: **Elastic reflection waveform inversion**

ABSTRACT

Full waveform inversion (FWI) is a highly nonlinear problem due to the complex reflectivity of the Earth, and this nonlinearity only increases under the more expensive elastic assumption. In elastic media, we need a good initial P-wave velocity and even a better initial S-wave velocity models with accurate representation of the low model wavenumbers for FWI to converge. However, inverting for the low wavenumber components of P- and S-wave velocities using reflection waveform inversion (RWI) with an objective to fit the reflection shape, rather than produce reflections, may mitigate the limitations of FWI. Because FWI, performing as a migration operator, is in preference of the high wavenumber updates along reflectors. We propose an elastic RWI that inverts for both the low wavenumber and perturbation components of the P- and S-wave velocities. To generate the full elastic reflection

wavefields, we derive an equivalent stress source made up by the inverted model perturbations and incident wavefields. We update both the perturbation and propagation parts of the velocity models in a nested fashion. Applications on synthetic isotropic models and field data show that our method can efficiently update the low and high wavenumber parts of the models.

INTRODUCTION

Full waveform inversion (FWI) was first introduced to our community with an acoustic approximation (Tarantola, 1984). Inverting for P-wave velocity (and its impedance) was regarded as the primary goal of waveform inversion, and thus was the main focus of the research effort and inversion implementations over the past thirty years (Tarantola, 1984; Plessix et al., 1995; Biondi and Symes, 2004; Hou and Symes, 2015; Choi and Alkhalifah, 2015). However, there is no question that the elastic assumption is a more accurate representation of the properties of seismic waves in the subsurface. The real subsurface contains more information that is far beyond the reach of acoustic inversion, even under the isotropic assumption. With the rise of FWI and its possible use in delineating reservoirs, the elastic description of the Earth drew a lot of attention lately, which we now refer to as Elastic full waveform inversion (EFWI)(Tarantola, 1986). The introduction of EFWI allowed its later application to real data problems by Mora (1987) and Crase et al. (1990) with mixed results. We also devoted our attention to the latest development of multi-parameter inversion (Operto et al., 2013), which included the challenges of parameter trade-off, inversion strategy and parameterization (Guitton and Alkhalifah, 2016; Wang et al., 2015; Oh and Alkhalifah, 2016), as the EFWI approach is still under development. Such studies present an illustration of the opportunities in using EFWI with respect to the acquisition design.

From the imaging perspective, the objective of FWI is to eliminate our historic practice of separating the propagation and reflectivity parts of the velocity model, and to combine them into a single, possibly high resolution model representing the Earth with accurate propagation and reflectivity properties. Thus, FWI is highly nonlinear because the complexity of the earth reflectivity is now part of the velocity model and the nonlinearity

further increases in the case of inverting multi-component data for P- and S-wave velocities. Though FWI has been successful in using refractions to build a high-resolution model for shallow earth (Choi and Alkhalifah, 2015), the limited bandwidth and aperture hinder its abilities in utilizing reflections, especially deep ones. Under these practical limitations, a reliable estimation of the background model, like migration velocity analysis (MVA) (Biondi and Symes, 2004; Sava et al., 2005; Symes, 2008) or image-based traveltime tomography (Clément et al., 2001) is required by the regular gradient based FWI methods, to achieve a natural transition from the low wavenumbers to the higher ones (Tarantola, 1984; Alkhalifah and Wu, 2016). Mora (1989) stated that inversion is a combination of migration and reflection tomography, which provide different wavenumbers of the model. Then Clément et al. (2001), based on the work of Plessix et al. (1995), implemented the MBTT formulation to build a background slowness model that gives the correct phase information. Based on these previous developments, Xu et al. (2012) suggested a workflow to invert for smooth models using the predicted P-wave reflections generated by a migration/demigration process, referred to as reflection waveform inversion (RWI). In this case, the objective is to find the long wavelength components of the velocity model necessary to image such reflections. This approach is a good stepping stone for FWI, as FWI needs a reasonable (depending on the minimum frequency) description of the kinematics of the wavefield embedded in the initial velocity model. A similar scope was exhibited by Staal and Verschuur (2013) in their implementation of joint migration inversion (JMI) (Berkhout, 2012), which generates a smooth velocity model while updates reflectivity. RWI can be implemented either in time or frequency domain with different workflows (Wang et al., 2013; Wu and Alkhalifah, 2014; Brossier et al., 2015), but the one thing in common between these implementations is that the property of demigrated reflections are highly sensitive to the image quality. In order

to achieve a better fit of the data, the image requires a true amplitude migration process that can be achieved with a least-squares optimization. Wu and Alkhalifah (2015), thus, proposed a new optimization problem, where they invert for both the background model and perturbations simultaneously.

For EFWI, which is a multi-parameter inversion problem, an accurate description of the kinematic component of the P- and S-wavefields is needed to mitigate the high nonlinearity. Considering the lower velocity (sometimes much lower than P-wave velocity) of the S-wave model and a relatively smaller scattering angle of PS converted waves, S-wave velocity model inversion is exposed mainly to higher wavenumber updates (Virieux and Operto, 2009; Prieux et al., 2013). Thus, optimizing the low wavenumber components for the S-wave velocity to avoid EFWI converging to local minima becomes even more challenging. Also, the acoustic migration/demigration process will definitely fail in the elastic case to reproduce a full reflection wavefield that wisely describes those events in multi-component data. Instead of doing so, we introduce an equivalent stress source located at the model perturbations, which is derived from the work of Wu and Zheng (2014). It is a nonlinear operator which includes the internal and surface-related multiples. The task of finding this long wavelength S-wave velocity model will be left to our newly proposed RWI.

In this paper, we split the regular elastic model parameters into slowly varying background and perturbation (reflectivity) parts and solve the nonlinear inversion problem for both of them. We use a nonlinear objective function including diving waves and reflections, similar to the work of Alkhalifah and Wu (2016). By doing so, the gradient with respect to the model background naturally takes into account the standard FWI kernel along the diving waves and RWI terms along reflection wavepaths. We will use a simple three-layer model for a gradient analysis. Then, we test our ERWI approach on a small section of

the Marmousi model, starting with a linearly increasing velocity model. Since optimization for the perturbation components is joint in our inversion, acting as an alternative to true amplitude migration, it will be utilized to improve the resolution of the inverted models. To generate scattered P- and S-wavefields, we apply our equivalent stress sources based on the inverted perturbations. The scatterers are no longer regarded as a single scatterer, thus no Born approximation is assumed in modeling the reflections. The final inverted model is composed of the optimized perturbation and the background. Compared with regular EFWI, our results present even higher resolution. Finally, an application on a Volve OBC dataset shows that our approach can provide a reasonably good inversion results. Both the Marmousi and real data examples show the ability of our method in recovering low wavenumber models, meanwhile end up with higher resolution results.

OPTIMIZATION OF STANDARD ACOUSTIC RWI

Conventional full waveform inversion attempts to find a model solution that minimizes the L2-norm misfit between the modeled data and observed data. It is classically defined as

$$\min \ E_{FWI}(\mathbf{m}) = \sum_{s,r} \frac{1}{2} \int dt |\mathbf{u}(\mathbf{x}_r, t) - \mathbf{d}(\mathbf{x}_r, t)|^2, \tag{1}$$

where $\mathbf{d}(\mathbf{x}_r, t)$ is the data observed at the receiver locations $\mathbf{x}_r$, $\mathbf{u}$ is the modeled wavefield associated with estimated model parameter. Since the gradient calculation of the classic objective function is closely related to reverse time migration (RTM), FWI tends to recover the high-resolution reflectivity parts of the model with limited bandwidth and size of the data survey, as compared to those updates with respect to low wavenumber components. Thus, in practice a good starting model that contains the kinematic information is required for a successful implementation of FWI; missing that information will possibly lead to

the notorious cycle-skipping problem. Xu et al. (2012) and Zhou et al. (2012), based on previous works of Plessix et al. (1995) and Clément et al. (2001), introduced reflection waveform inversion (RWI), which can greatly improve the low wavenumber model building process similar to MVA but in data domain.

The standard RWI produces reflections from a migration and demigration process. Physically, seismic reflections are generated from the contrast part of the velocity (or impedance). The initial model of FWI often contains low wavenumber components (as compared with the wavelength of injected wavefield). Thus, the FWI model can hardly generate any recognizable reflection at the early stage until the updated model itself includes high enough wavenumbers that induces reflections. However, since the low wavenumber and high wavenumber components are well decoupled (Clément et al., 2001; Xu et al., 2012), we can utilize the migration and demigration process to generate reflections (Symes and Kern, 1994). The process to generate reflection wavefields (Biondi and Almomin, 2014) can be expressed as

$$\frac{\partial^2 u}{\partial t^2} - v^2 \nabla^2 u = f, \tag{2}$$

$$\frac{\partial^2 \delta u}{\partial t^2} - v^2 \nabla^2 \delta u = I \cdot u, \tag{3}$$

where v is the low wavenumber components of velocity model, u is the wavefield for the low wavenumber model, f is the actual source; δu is the perturbed reflection wavefield and I is the depth domain migration of reflections. The second line, equation 3, is the demigration process. The reflections produced by this process can always match those reflections of the observed data in the near offset, which to some extent can mitigate the cycle-skipping problem. Considering the Fréchet derivative of δu with respect to the background velocity

v, the gradient can be calculated by:

$$\nabla_v E_{FWI} = -\sum \int dt(\Psi \nabla^2 \delta u + \delta \Psi \nabla^2 u), \tag{4}$$

where ∇^2 is Laplacian operator in the space domain, Ψ is the adjoint wavefield. Conventional FWI updates low wavenumber components of model in the shallow zone relying on direct and diving waves, while RWI provides a different low wavenumber update for the deeper parts of the model along the reflection wavepaths. The first and second terms in equation 4 correspond to the wavepaths on receiver and source sides, respectively. They are shown in Figures 1a and 1b by summation over receivers for one shot.

As we can see from Figures 1a and 1b, the gradient of RWI mainly provides a smooth update. Since true amplitude migration is needed, Alkhalifah and Wu (2016) suggested inverting for both the reflectivity and velocity background with a newly introduced objective function:

$$\min \ E_{RWI}(\mathbf{m}) = \sum_{s,r} \frac{1}{2} \int dt |\mathbf{u}(\mathbf{x}_r, t) + \delta \mathbf{u}(\mathbf{x}_r, t) - \mathbf{d}(\mathbf{x}_r, t)|^2, \tag{5}$$

where $\mathbf{u}(\mathbf{x}_r, t) + \delta \mathbf{u}(\mathbf{x}_r, t)$ is the total wavefield. Using this objective function, we are matching both the diving waves and reflections, compared to only matching the reflections in RWI. Similar to FWI, matching the whole wavefield will admit a diving wave update into the gradient. Zhou et al. (2015) also claimed the importance of diving wave in their proposed approach, namely joint FWI.

OBJECTIVE FUNCTION AND PERTURBED WAVEFIELDS WITH EQUIVALENT SOURCE

Elastic waveform inversion is of higher nonlinearity compared to the acoustic case. The high nonlinearity is caused by the missing low wavenumbers in the initial model for both

P and S waves. Considering that the update for S-wave velocity in FWI injects intrinsically even higher wavenumbers than P waves regarding the lower propagation velocity, the task of recovering low wavenumber components becomes more daunting. RWI is a general inversion method for low wavenumber components of the velocity model and can be implemented either in time or frequency with different workflows (Wang et al., 2013; Alkhalifah and Wu, 2016). In order to achieve a better fit of the data reflections, it is a common affair that the image used to emit reflections requires a true amplitude migration process, such as a least squares type of optimization. In the elastic situation, we need a more accurate description of the reflection wavefield beyond the migration and demigration process. Indeed, generating perturbed wavefields in elastic media requires more than the seismic image (P- or S-wave image). For acoustic RWI, PP- image is the only parameter to approximate those reflectors, while for elastic models, elastic imaging workflows can output four cross-correlation components (Yan and Sava, 2008; Duan and Sava, 2015; Yang et al., 2015), or two-component image perturbations (Duan et al., 2017), alternatively. The latter which represents the high wavenumber components of the models has a more clearer physical meaning and fortunately it can be optimized naturally within the EFWI framework. In addition, Rocha et al. (2017) are able to obtain one image for elastic inversion (not knowing what the image really represents physically).

We define our elastic model parameters in the isotropic case as

$$\alpha = \frac{\lambda + 2\mu}{\rho} \quad \text{and} \quad \beta = \frac{\mu}{\rho}, \tag{6}$$

and split them into low wavenumber components (background) and perturbation parts respectively:

$$\alpha = \alpha_0 + \delta\alpha \quad \text{and} \quad \beta = \beta_0 + \delta\beta, \tag{7}$$

where λ and μ are the Lamé constants, ρ is the density of the medium.

We assume the total wavefield can also be decoupled into the wavefield propagating in slowly varying background media and the scattered from the model perturbations:

$$\mathbf{u}_{total} = \mathbf{u} + \delta\mathbf{u}. \tag{8}$$

It satisfies a coupled system of equations (with constant density):

$$\begin{cases} \dfrac{\partial^2(u_x+\delta u_x)}{\partial t^2} = \dfrac{1}{\rho}\left(\dfrac{\partial(\tau_{xx}+\delta\tau_{xx})}{\partial x} + \dfrac{\partial(\tau_{xz}+\delta\tau_{xz})}{\partial z}\right), \\ \dfrac{\partial^2(u_z+\delta u_z)}{\partial t^2} = \dfrac{1}{\rho}\left(\dfrac{\partial(\tau_{zz}+\delta\tau_{zz})}{\partial z} + \dfrac{\partial(\tau_{xz}+\delta\tau_{xz})}{\partial x}\right), \end{cases} \tag{9}$$

where

$$\begin{cases} \tau_{xx}+\delta\tau_{xx} = (\alpha_0+\delta\alpha)\left(\dfrac{\partial u_x}{\partial x} + \dfrac{\partial \delta u_x}{\partial x}\right) + (\alpha_0+\delta\alpha-2\beta_0-2\delta\beta)\left(\dfrac{\partial u_z}{\partial z} + \dfrac{\partial \delta u_z}{\partial z}\right), \\ \tau_{zz}+\delta\tau_{zz} = (\alpha_0+\delta\alpha)\left(\dfrac{\partial u_z}{\partial z} + \dfrac{\partial \delta u_z}{\partial z}\right) + (\alpha_0+\delta\alpha-2\beta_0-2\delta\beta)\left(\dfrac{\partial u_x}{\partial x} + \dfrac{\partial \delta u_x}{\partial x}\right), \\ \tau_{xz}+\delta\tau_{xz} = (\beta_0+\delta\beta)\left(\dfrac{\partial\,(u_x+\delta u_x)}{\partial z} + \dfrac{\partial\,(u_z+\delta u_z)}{\partial x}\right), \end{cases} \tag{10}$$

where $\mathbf{u}$ is the displacement vector and τ is the stress tensor. This system of equations can be solved using a staggered-grid finite difference approach.

To calculate the perturbed wavefields, we can eliminate the terms related to the background model, in which $\mathbf{u}$ and τ satisfy:

$$\begin{aligned} \frac{\partial^2\mathbf{u}}{\partial t^2} &= \frac{1}{\rho}\nabla\tau, \\ \tau &= \mathbf{m}_0 \,:\, \nabla\mathbf{u}, \end{aligned} \tag{11}$$

where $\mathbf{m}_0$ is the elastic tensor composed of low wavenumber model parameters α_0 and β_0 and : denotes the Frobenius inner product. Finally the perturbed reflection wavefield is given by

$$\begin{cases} \dfrac{\partial^2\delta u_x}{\partial t^2} = \dfrac{1}{\rho}\left(\dfrac{\partial\delta\tau_{xx}}{\partial x} + \dfrac{\partial\delta\tau_{xz}}{\partial z}\right), \\ \dfrac{\partial^2\delta u_z}{\partial t^2} = \dfrac{1}{\rho}\left(\dfrac{\partial\delta\tau_{zz}}{\partial z} + \dfrac{\partial\delta\tau_{xz}}{\partial x}\right), \end{cases} \tag{12}$$

and if we look into Hooke's law that relates stress and strain, we can derive the perturbations in stress tensors:

$$\begin{cases} \delta\tau_{xx} = (\alpha_0 + \delta\alpha)\dfrac{\partial \delta u_x}{\partial x} + (\alpha_0 + \delta\alpha - 2\beta_0 - 2\delta\beta)\dfrac{\partial \delta u_z}{\partial z} + \tilde{\tau}_{xx}, \\ \delta\tau_{zz} = (\alpha_0 + \delta\alpha - 2\beta_0 - 2\delta\beta)\dfrac{\partial \delta u_x}{\partial x} + (\alpha_0 + \delta\alpha)\dfrac{\partial \delta u_z}{\partial z} + \tilde{\tau}_{zz}, \\ \delta\tau_{xz} = (\beta_0 + \delta\beta)(\dfrac{\partial \delta u_x}{\partial z} + \dfrac{\partial \delta u_z}{\partial x}) + \tilde{\tau}_{xz}, \end{cases} \tag{13}$$

where $\tilde{\tau}_{ij}$ can be expressed as

$$\begin{cases} \tilde{\tau}_{xx} = \delta\alpha\left(\dfrac{\partial u_x}{\partial x} + \dfrac{\partial u_z}{\partial z}\right) - 2\delta\beta\dfrac{\partial u_z}{\partial z}, \\ \tilde{\tau}_{zz} = \delta\alpha\left(\dfrac{\partial u_x}{\partial x} + \dfrac{\partial u_z}{\partial z}\right) - 2\delta\beta\dfrac{\partial u_x}{\partial x}, \\ \tilde{\tau}_{xz} = \delta\beta\left(\dfrac{\partial u_x}{\partial z} + \dfrac{\partial u_z}{\partial x}\right), \end{cases} \tag{14}$$

which involves the displacement wavefields in background media (α_0 and β_0) and estimated model perturbations $\delta\alpha$ and $\delta\beta$. These stress components injected into the system of equations 13 perform the purpose of emitting reflections, which can be regarded as the equivalent sources, similar to the ones derived by Wu and Zheng (2014) in the acoustic case. Thus, $\delta\tau_{ij}$ here can be regarded as the stress tensor in the supposed entire model, free of the actual source at the surface, but alternatively includes an equivalent source $\tilde{\tau}_{ij}$ that only emits reflections at the model perturbations.

These are the exact expressions of perturbed wavefields, which is nonlinear with respect to model perturbations. Thus, the computed waveforms here not only contains primary reflections, but also multiples; there is no Born approximation. To illustrate the perturbed wavefields by our nonlinear formulation, we use a constant background model with two scatter perturbations in both P- and S-velocity located at the yellow dots in Figure 2a, in which the source location is indicated by a red star. Figures 2a and 2c show the elastic potentials of the entire wavefield and Figures 2b and 2d show the elastic potentials of the corresponding scatter wavefield reproduced by injecting our equivalent sources. As we can

see, the nonlinear approach offers an accurate description of perturbations imbedded in the entire wavefield.

Our objective function for ERWI is similar to the one Alkhalifah and Wu (2016) used: $\min E(\mathbf{m}) = \sum \frac{1}{2} \int_t |\mathbf{u}(\mathbf{x}_r, t) + \delta\mathbf{u}(\mathbf{x}_r, t) - \mathbf{d}(\mathbf{x}_r, t)|^2$. Here the data is multi-component displacement field that contains u_x and u_z and $\delta\mathbf{u}$ is nonlinear with respect to model perturbations. Others proposed to use cost functions of the correlation type in RWI (Xu et al., 2012; Zhou et al., 2012; Wu and Alkhalifah, 2015). Since we are doing a simultaneous inversion for both low wavenumber components and perturbations of model, we suggest a more flexible strategy in choosing the cost function depending on the decoupled features of these two components. For the high wavenumber components of the model, which control the dynamic features (amplitude) of the reflection waveform, we suggest using a standard L2-norm misfit function. The high sensitivity of this function with respect to the amplitude of the modeled reflections enables a more accurate estimation of the model perturbations. For the slowly varying background model, which mainly influences the kinematic features of reflection/transmission, its sensitivity with respect to the amplitude becomes relatively trivial as compared with the high wavenumber components. Thus, the misfit function should be less sensitive to amplitude but focus on the traveltime. We suggest the inner product function given by Choi and Alkhalifah (2012).

FEATURES OF NONLINEAR ERWI AND GRADIENT ANALYSIS

Compared to standard RWI, we reproduce the reflections using equivalent stress sources built from model perturbations. The model perturbations must be optimized to guarantee that modeled reflections have somewhat an inverse characteristic to the migration. In other words, the perturbed wavefield must fit the whole data when the velocity is accurate,

and fit the near-offset data only when the velocity is inaccurate. Thus, we invert for the perturbations and background models in a nested approach, instead of only inverting for the backgrounds. Using our suggested cost functions, we just need to make some changes to the adjoint sources when we transfer from one objective to another.

In our applications, we use an explosive source, which mainly produces pressure waves. The multi-component acquisition is dominated by P-waves and at larger offsets includes converted P- to S-waves. We can apply our equivalent stress sources using the inverted velocity perturbations and the incident displacement fields. After obtaining the scattered P- and S-wavefields, we calculate the gradients (see Appendix A) of the objective function with respect to $\alpha_0, \delta\alpha$ using the adjoint state method (Plessix, 2006):

$$\begin{aligned}\nabla_{\alpha_0} E_{RWI} = & - \sum_s \int dt \left(\tfrac{\partial}{\partial x} u_x + \tfrac{\partial}{\partial z} u_z\right)\left(\tfrac{\partial}{\partial x}\Psi_x + \tfrac{\partial}{\partial z}\Psi_z\right) \\ & + \left(\tfrac{\partial}{\partial x} u_x + \tfrac{\partial}{\partial z} u_z\right)\left(\tfrac{\partial}{\partial x}\delta\Psi_x + \tfrac{\partial}{\partial z}\delta\Psi_z\right) + \left(\tfrac{\partial}{\partial x}\delta u_x + \tfrac{\partial}{\partial z}\delta u_z\right)\left(\tfrac{\partial}{\partial x}\tilde{\Psi}_x + \tfrac{\partial}{\partial z}\tilde{\Psi}_z\right), \end{aligned} \tag{15}$$

$$\nabla_{\delta\alpha} E_{RWI} = - \sum_s \int dt \left(\tfrac{\partial}{\partial x} u_x + \tfrac{\partial}{\partial x}\delta u_x + \tfrac{\partial}{\partial z} u_z + \tfrac{\partial}{\partial z}\delta u_z\right)\left(\tfrac{\partial}{\partial x}\tilde{\Psi}_x + \tfrac{\partial}{\partial z}\tilde{\Psi}_z\right), \tag{16}$$

and for $\beta_0, \delta\beta$ is given by:

$$\begin{aligned}\nabla_{\beta_0} E_{RWI} = & - \sum_s \int dt\ 2\left(\tfrac{\partial}{\partial x} u_x \tfrac{\partial}{\partial x}\Psi_x + \tfrac{\partial}{\partial z} u_z \tfrac{\partial}{\partial z}\Psi_z\right) + \left(\tfrac{\partial}{\partial z} u_x + \tfrac{\partial}{\partial x} u_z\right)\left(\tfrac{\partial}{\partial z}\Psi_x + \tfrac{\partial}{\partial x}\Psi_z\right) \\ & + 2\left(\tfrac{\partial}{\partial x} u_x \tfrac{\partial}{\partial x}\delta\Psi_x + \tfrac{\partial}{\partial z} u_z \tfrac{\partial}{\partial z}\delta\Psi_z + \tfrac{\partial}{\partial x}\delta u_x \tfrac{\partial}{\partial x}\tilde{\Psi}_x + \tfrac{\partial}{\partial z}\delta u_z \tfrac{\partial}{\partial z}\tilde{\Psi}_z\right) \\ & + \left(\tfrac{\partial}{\partial z} u_x + \tfrac{\partial}{\partial x} u_z\right)\left(\tfrac{\partial}{\partial z}\delta\Psi_x + \tfrac{\partial}{\partial x}\delta\Psi_z\right) + \left(\tfrac{\partial}{\partial z}\delta u_x + \tfrac{\partial}{\partial x}\delta u_z\right)\left(\tfrac{\partial}{\partial z}\tilde{\Psi}_x + \tfrac{\partial}{\partial x}\tilde{\Psi}_z\right), \end{aligned} \tag{17}$$

$$\begin{aligned}\nabla_{\delta\beta} E_{RWI} = & - \sum_s \int dt\ 2\left(\tfrac{\partial}{\partial x} u_x + \tfrac{\partial}{\partial x}\delta u_x\right)\tfrac{\partial}{\partial x}\tilde{\Psi}_x + 2\left(\tfrac{\partial}{\partial z} u_z + \tfrac{\partial}{\partial z}\delta u_z\right)\tfrac{\partial}{\partial z}\tilde{\Psi}_z \\ & + \left(\tfrac{\partial}{\partial z} u_x + \tfrac{\partial}{\partial z}\delta u_x + \tfrac{\partial}{\partial x} u_z + \tfrac{\partial}{\partial x}\delta u_z\right)\left(\tfrac{\partial}{\partial z}\tilde{\Psi}_x + \tfrac{\partial}{\partial x}\tilde{\Psi}_z\right), \end{aligned} \tag{18}$$

where Ψ is the adjoint displacement field propagated in background model, $\tilde{\Psi}$ is the adjoint

wavefield that satisfies the elastic wave equation with an assumed true model, $\alpha_0 + \delta\alpha$ and $\beta_0 + \delta\beta$, $\delta\Psi$ is the field produced by perturbing $\tilde{\Psi}$ at the inverted high wavenumber models. It can be noticed that $\tilde{\Psi} = \Psi + \delta\Psi$ from Appendix A. Here, the diving waves are generated and naturally included in the inversion. They provide major contributors to the background updates in the shallow part of the model, thus, they complement the low wavenumber updates of the deeper zones provided by conventional RWI.

Therefore, the workflow of our suggested ERWI is given in Table 1.

NUMERICAL EXAMPLES

Three-layer model

First, we apply our ERWI on a simple elastic model shown in Figures 3a and 3b and analyse the gradients. For simplicity, we fix the P- to S-velocity ratio and use constant initial models (2.5 km/s and 1.44 km/s) for P- and S-wave velocities. Our acquisition contains 32 shots distributed regularly on the surface and 320 fixed receivers every 15.24 m. The source function is given by a Ricker's wavelet with a peak frequency of 8 Hz and a frequency band is between 0 and 20 hz. The gradients for elastic parameters α_0 and β_0 using the perturbed reflections are shown in Figures 3c and 3d. Alternatively, including the diving wave terms, the gradients for α_0 and β_0 are shown in Figures 3e and 3f. The gradients exhibit reasonably long wavelengths for α_0 and β_0. As we can see from Figures 3c and 3d, our ERWI method provides a very smooth gradients for both α_0 and β_0 models and correct directions of updates (opposite for the two layers). However, the updates are focused on the deeper zone because they update the low wavenumber components of models for imaging the reflections. After including the diving wave term, the updates include the

anomaly in the shallow zone. Thus, our new proposed method improves the background optimization by taking into account the two major sources for low wavenumber updates.

Marmousi model

Next, we test our method on a small section of the Marmousi model. The goal is to obtain a high resolution estimates for P- and S-wave velocities. Figures 4a and 4c show the true elastic model. We extend the water layer depth of the actual Marmousi in order to mitigate the source effects. The source function, which contains pressure stress only, is given by a Ricker's wavelet with a peak frequency of 8 Hz. There are 32 shots with 152 m interval and 320 receivers evenly distributed on the surface that are fixed for each shot. The initial model is linearly increasing except in the extended layer (Figures 4b and 4d), in which we keep the velocity fixed during the inversion. We use here L-BFGS method for the optimization and also apply a fixed ratio to the step lengths of α and β updates. First, we optimize for the reflectivity parts of elastic model $\delta\alpha$ and $\delta\beta$ using the L2-norm objective function on near-offset data. The low wavenumber estimates of P- and S-wave velocities using our nested approach are shown in Figures 5a and 5b, respectively. As we can see, our suggested ERWI successfully recovers the low wavenumber structures. Adding the optimized perturbations to the inverted backgrounds we obtain the models shown in Figures 5c and 5d. For comparison, we apply regular EFWI starting from the velocities in Figures 4b and 4d and obtain the inverted models shown in Figures 5e and 5f. Because we use the global correlation objective function when we optimize the background velocities, the same objective function is applied to EFWI followed by the same amount of iteration using the L2-norm objective function. We note that the models obtained by adding the inverted perturbations to the backgrounds look plausible and more promising to high resolution inversion. This result also implies that

in some cases, we do not need to include the added cost of EFWI that relies on the result of RWI.

To further test the performance of our approach in recovering low wavenumber models, we filter out of the data frequencies below 3 Hz to imitate practical situations. The other parameters of the experiment are the same. Using only the direct and diving waves, the absence of low frequencies will deteriorate the optimization of the background models because the corresponding updates only cover the relatively shallow zone, while our proposed ERWI does not suffer from such limitation. The entire velocity models ($\alpha_0 + \delta\alpha$ and $\beta_0 + \delta\beta$) estimated using our method are shown in Figures 6a and 6c. The velocity profiles in the middle of the model are shown in Figures 7a and 7b. We again apply regular EFWI that starts from the velocities in Figures 4b and 4d and obtain the inverted models shown in Figures 6b and 6d. In EFWI, we use the same procedure as the experiment above that keeps the entire frequency band. This time the regular EFWI fails to obtain a reasonable solution because of the cycle-skipping problem, even though we use the global correlation objective function that helps mitigate this problem and better retrieves low wavenumber models. As we can see in Figures 7a and 7b, EFWI can only fit the P-wave velocity at the shallow part of the model and is incapable of giving a reasonable S-wave velocity; while our ERWI achieves good estimates for both P- and S-wave velocities. Thus, our optimization approach yields a better background models even without the low frequencies in the data, especially for the S-wave velocity. The inverted $\delta\alpha$ and $\delta\beta$ using our approach are shown in Figures 8c and 8d and the true perturbations are shown in Figures 8a and 8b. The true and the inverted ones match well with each other. In addition, our method performs very well in combining the propagation and reflectivity parts of velocity model. Figure 9 shows the convergence curve of our ERWI. It takes 3 outer loops with 20 iterations of updating

perturbations and 10 iterations of updating backgrounds in each outer loop.

Volve OBS data

Finally, we apply our approach on a 2D slice with a two-component dataset extracted from a 3D OBS survey of Volve field, located in the Norwegian North Sea. The field is characterized by a reservoir structure (Szydlik et al., 2007). The data provided have 12 parallel cables with 240 receivers in each cable and the vertical and horizontal components of the data were processed, respectively, to mainly contain PP and PS information. The 2D dataset is extracted from an inline close to the middle of the structure. The 240 receivers are evenly distributed at the middle of the survey, with a 25 m interval. We use 121 shots with a 100 m interval. We apply a power gain to the data to match the energy of 2D modeling. We invert for the source wavelet by back-propagating data at the receiver to its true source location (Plessix, 2006; Lailly, 1983).

The tomography models provided are shown in Figures 10a and 10c. We smooth them three times with a window size of 500 m by 500 m as the initial P- and S-wave velocity, which are shown in Figures 10b and 10d, respectively. The initial models smear out most of the structures and only keep the water layer with an average depth of 90 m. The model size is 12.3 km in the horizontal direction and 4.25 km in depth. In our inversion we use three stages with different bandwidths. At the first stage, we bandpass the data with 2 to 4 Hz to guarantee smooth updates and mitigate the cycle-skipping. To optimize the perturbations of the models, we use an L2-norm misfit function on the near-offset data. After we obtain the inverted perturbations, we apply the global correlation objective function to the data with offset larger than 500 m to update the background models. At the second stage, we

apply the same strategy, with the data bandpass between 2 and 6 Hz. The nested inversion runs three outer loops in the first stage, two outer loops in the second stage and one loop in the third. The optimized perturbations and background models at the last stage are carried out to the current one as initial models. The vertical component of the original shot gather and the predicted data after the second stage are shown in Figure 11a side by side. The predicted data match well with the main reflection events in the observed one, while it leaves some less dominant events unmatched. We attribute these unmatched ones to two possible factors: first, the missing PS and PP events in the provided data (though it is not muted completely); second, the internal multiples that appear as more events in our prediction but have been suppressed in the provided data. The first one may lead to some artifacts in the perturbations since we are trying to match some reflections of incomplete components. The second one, which is caused by the conflict between our nonlinearity operator and the artificial muting of multiples, may induce some more artifacts as the inversion is struggling with some unphysical mismatch in the data. Besides the incomplete components in the data, the survey brings some geometry artifacts into the model perturbations because the receivers only cover the middle portion of the model (between 3 km and 9 km), compared to the 12 km full coverage of the shot line. Fortunately, we utilize the global correlation objective function in optimizing the background, which reduces the impact of such data mismatch. Figure 11b shows the data match after the third stage, in which the data have a bandpass between 2 and 8 Hz. The predicted gather is improved and even matches the phases of some later arrivals. In addition, there might be other reasons for residuals in the data, that is the anisotropic nature of the medium, which is ignored here.

Figures 12a and 12c show the estimated backgrounds of P- and S-wave velocities using our nested approach, respectively. The inversion tends to admit reasonable long wavelength

models, especially for the S-wave velocity. Adding the optimized perturbations to the inverted backgrounds, we obtain the entire models $\alpha_0 + \delta\alpha$ and $\beta_0 + \delta\beta$. Figures 12b and 12d show the inverted P- and S-wave velocity models, respectively. The inverted P- and S-wave velocity models have consistent layers at the shallow area and generally similar structures at the deeper parts. S-wave perturbations show better continuity in these shallow layers. The missing components in the data indeed deteriorate the S-wave perturbations, especially in the deeper zone. From the inverted P- and S-wave velocities we can find indications of velocity changes resulting in a thick layer between 2.6 and 2.9 km depth followed by a low velocity zone between 2.9 and 3.2 km depth, which could be the expected subchalk reservoir.

The acoustic reverse time migrations (RTM), corresponding to the vertical component of the data with a bandpass of 2 to 30 Hz, are shown in Figures 13a and 13b, which are computed using the initial smoothed tomography and our ERWI P-wave velocity, respectively. The acoustic image obtained using our ERWI velocity has a more flat posture above the chalk layer compared to the one calculated using the smoothed tomography velocity; the image at 2.2 km depth is deblurred and also the events at the deeper zone (below 3 km) are a bit more continuous after inversion.

To evaluate the images calculated by our inverted model, we generate the angle domain common image gathers (ADCIGs) for elastic PP-images. Figures 14a and 14b show the PP-image gathers of the initial smoothed tomography model and the ERWI model, respectively. We notice that the inversion result indeed flattens the PP-ADCIGs of some events, including the reflectors at 1.8 km, 2.4 km and even 3.0 km depth (marked by the yellow arrows). Because of the strong reflection at 2.5 km depth, the images below are much weaker. This, to some extent, verifies the accuracy of our model estimations.

DISCUSSION

Elastic reflection waveform inversion greatly improves the background estimates of the elastic models. Our numerical model experiments show that even when using data without frequencies below 3 Hz, our suggested ERWI can still achieve a reasonable low wavenumber updates for the background model optimization. However, when we turn to data with more limited offset and higher frequency band, we need to combine our approach with other strategies, like a multi-stage approach based on frequency continuation (from low frequencies to higher ones), in order to help reduce the high nonlinearity. In other words, our method still favors data with larger bandwidth, especially low frequency components, and far offset, which provides multi-scale updates that can better fill the wavenumber gap between MVA and reflectivity inversion (Claerbout, 1985).

Though our approach obtains better estimates of low wavenumber models compared to FWI, it is still suffers from cycle skipping when the initial guess of the model is reasonably poor. However, we experience the opportunity to mitigate cycle-skipping in our ERWI. Specifically, since the migration/demigration steps produce data with good fit of the near-offset observed data, we impose a simple corollary that if we add far offsets gradually to the optimization using RWI, we may avoid getting into local minimum at early stage.

As we can see from equations 15 – 18, the gradients with respect to model perturbations share several terms with those related to updating the model backgrounds. These are diving wave terms, causing cross-talk between our multi-parameter optimization. Since we prefer consistent high wavenumber updates for perturbations, we can solve this problem either using a scattering-angle based filter (Alkhalifah, 2015) to optimize the gradients or we can just drop the diving wave terms in the gradient calculations of the perturbations.

Theoretically, we will always benefit in the shallow part from the diving wave terms, which are already included in the background updates. As the shallow zone of the inverted models approach the true solution, the diving wave terms will gradually decay in influence.

CONCLUSION

In our elastic RWI, we implement a nonlinear inversion for low and high wavenumber components of the P- and S- wave models in a nested approach. The low wavenumber components are recoverable from the reflections generated by the equivalent stress sources and the diving waves. Compared to regular RWI, retrieving low wavenumber models good enough for a subsequent EFWI, we obtain optimization for both the perturbation and the background models simultaneously and avoid the two-step inversion by adding the inverted perturbations to the backgrounds. As we demonstrated with the Marmousi example, it enables us to obtain high resolution models. Our method also succeeds in obtaining a reliable low wavenumber description of model parameters with the absence of low frequency data, which is a tough mission for regular EFWI.

ACKNOWLEDGMENTS

The authors would like to thank Statoil ASA and the Volve license partners ExxonMobil E&P Norway AS and Bayerngas Norge AS, for the release of the Volve data. The views expressed in this paper are the views of the authors and do not necessarily reflect the views of Statoil ASA and the Volve field license partners. The authors would like to thank Marianne Houbiers from Statoil, who gave some very helpful suggestions and corrections. We also appreciate the suggestions provided by Antoine Guitton, Vincent Prieux from CGG, Jiubing

Cheng and also two anonymous reviewers as part of the review process of this paper. We also thank KAUST for its support and we thank the SWAG group for collaborative environment, especially Zedong Wu and Juwon Oh for their helpful suggestions and discussions.

APPENDIX A

GRADIENT CALCULATION

We derive the gradient of the objective function with respect to background model m_0 (α_0, β_0) and model perturbation δm ($\delta\alpha$, $\delta\beta$) following a similar strategy to Ma and Hale (2013) and Wu and Alkhalifah (2015):

$$dE(\mathbf{u},\delta\mathbf{u}) = \frac{\partial E(\mathbf{u},\delta\mathbf{u})}{\partial \mathbf{m}_0} d\mathbf{m}_0 + \frac{\partial E(\mathbf{u},\delta\mathbf{u})}{\partial \delta\mathbf{m}} d\delta\mathbf{m}, \tag{A-1}$$

$$= \sum_s \int_t dt \left(\mathbf{u}(\mathbf{m}_0) + \delta\mathbf{u}(\mathbf{m}_0,\delta\mathbf{m}) - \mathbf{d}\right)\left(d\mathbf{u}(\mathbf{m}_0) + d\delta\mathbf{u}(\mathbf{m}_0,\delta\mathbf{m})\right), \tag{A-2}$$

where $\sum$ is summation over space, d means a small perturbation of function (or variable). From equation 11, the elastic displacement field satisfies:

$$\mathbf{u}_{tt} = \nabla\cdot(\mathbf{m}_0 : \nabla\mathbf{u}) + \mathbf{f}, \tag{A-3}$$

and also the reflection wavefield satisfies:

$$\delta\mathbf{u}_{tt} = \nabla\cdot((\mathbf{m}_0 + \delta\mathbf{m}) : \nabla\delta\mathbf{u}) + \nabla\cdot(\delta\mathbf{m} : \nabla\mathbf{u}), \tag{A-4}$$

where : is the Frobenius inner product, $\mathbf{f}$ is a known independent function. The perturbation of $\mathbf{u}$ is then given by:

$$d\mathbf{u}_{tt} = \nabla\cdot\nabla\mathbf{u} : d\mathbf{m}_0 + \nabla\cdot(\mathbf{m}_0 : \nabla d\mathbf{u}), \tag{A-5}$$

and perturbation of $\delta\mathbf{u}$ is given by:

$$d\delta\mathbf{u}_{tt} = \nabla\cdot\nabla\delta\mathbf{u} : (d\mathbf{m}_0 + d\delta\mathbf{m}) + \nabla\cdot((\mathbf{m}_0+\delta\mathbf{m}) : \nabla d\delta\mathbf{u}) \tag{A-6}$$

$$+\nabla\cdot\nabla\mathbf{u} : d\delta\mathbf{m} + \nabla\cdot(\delta\mathbf{m} : \nabla d\mathbf{u}), \tag{A-7}$$

thus, the perturbation for $\mathbf{u}$ is

$$d\mathbf{u} = \left(\frac{\partial^2}{\partial t^2} - \nabla\cdot(\mathbf{m}_0 : \nabla)\right)^{-1} \nabla\cdot\nabla\mathbf{u} : d\mathbf{m}_0, \tag{A-8}$$

and for reflection wavefield $\delta\mathbf{u}$ is

$$d\delta\mathbf{u} = \left(\frac{\partial^2}{\partial t^2} - \nabla\cdot((\mathbf{m}_0+\delta\mathbf{m}) : \nabla)\right)^{-1} \cdot \tag{A-9}$$

$$\left(\nabla\cdot\nabla\delta\mathbf{u} : (d\mathbf{m}_0 + d\delta\mathbf{m}) + \nabla\cdot\nabla\mathbf{u} : d\delta\mathbf{m} + \nabla\cdot(\delta\mathbf{m} : \nabla d\mathbf{u})\right). \tag{A-10}$$

We substitute $d\mathbf{u}$ and $d\delta\mathbf{u}$ into the equation, and define

$$\boldsymbol{\Psi} = \left(\frac{\partial^2}{\partial t^2} - \nabla\cdot(\mathbf{m}_0 : \nabla)\right)^{-T} (\mathbf{u} + \delta\mathbf{u} - \mathbf{d}), \tag{A-11}$$

and

$$\tilde{\boldsymbol{\Psi}} = \left(\frac{\partial^2}{\partial t^2} - \nabla\cdot((\mathbf{m}_0+\delta\mathbf{m}) : \nabla)\right)^{-T} (\mathbf{u} + \delta\mathbf{u} - \mathbf{d}), \tag{A-12}$$

where $\boldsymbol{\Psi}$ and $\tilde{\boldsymbol{\Psi}}$ is the adjoint wavefield for back propagating the data residual in the background and supposedly entire media, T is adjoint operation. Then we get the perturbation of cost function:

$$dE(\mathbf{u},\delta\mathbf{u}) = \sum_s \int_t dt\, \nabla\boldsymbol{\Psi}\cdot\nabla\mathbf{u} : d\mathbf{m}_0 + \nabla\tilde{\boldsymbol{\Psi}}\cdot\nabla\delta\mathbf{u} : d\mathbf{m}_0 + \nabla\delta\tilde{\boldsymbol{\Psi}}\cdot\nabla\mathbf{u} : d\mathbf{m}_0 \tag{A-13}$$

$$+\nabla\tilde{\boldsymbol{\Psi}}\cdot\nabla\delta\mathbf{u} : d\delta\mathbf{m} + \nabla\tilde{\boldsymbol{\Psi}}\cdot\nabla\mathbf{u} : d\delta\mathbf{m}, \tag{A-14}$$

where

$$\delta\tilde{\boldsymbol{\Psi}} = \left(\frac{\partial^2}{\partial t^2} - \nabla\cdot(\mathbf{m}_0 : \nabla)\right)^{-T} (\delta\mathbf{m} : \nabla\tilde{\boldsymbol{\Psi}}). \tag{A-15}$$

This equation presents the adjoint wavefield with the Green's function generated from the equivalent stress sources for the low wavenumber background. Transforming the elastic tensor to Lamé parameters, we have the gradient of our cost function with respect to λ:

$$\nabla E_\lambda = \sum_s \int_t dt\, (\nabla \cdot \mathbf{\Psi})(\nabla \cdot \mathbf{u}) + (\nabla \cdot \tilde{\mathbf{\Psi}})(\nabla \cdot \delta\mathbf{u}) + (\nabla \cdot \delta\tilde{\mathbf{\Psi}})(\nabla \cdot \mathbf{u}), \tag{A-16}$$

and $\delta\lambda$:

$$\nabla E_{\delta\lambda} = \sum_s \int_t dt\, (\nabla \cdot \tilde{\mathbf{\Psi}})(\nabla \cdot \delta\mathbf{u}) + (\nabla \cdot \tilde{\mathbf{\Psi}})(\nabla \cdot \mathbf{u}), \tag{A-17}$$

and for μ we have:

$$\nabla E_\mu = \frac{1}{2}\sum_s \int_t dt \left(\nabla\mathbf{\Psi} + (\nabla\mathbf{\Psi})^T\right) : \left(\nabla\mathbf{u} + (\nabla\mathbf{u})^T\right) \tag{A-18}$$

$$+\left(\nabla\tilde{\mathbf{\Psi}} + (\nabla\tilde{\mathbf{\Psi}})^T\right) : \left(\nabla\delta\mathbf{u} + (\nabla\delta\mathbf{u})^T\right) + \left(\nabla\delta\tilde{\mathbf{\Psi}} + (\nabla\delta\tilde{\mathbf{\Psi}})^T\right) : \left(\nabla\mathbf{u} + (\nabla\mathbf{u})^T\right), \tag{A-19}$$

and $\delta\mu$:

$$\nabla E_{\delta\mu} = \frac{1}{2}\sum_s \int_t dt \left(\nabla\tilde{\mathbf{\Psi}} + (\nabla\tilde{\mathbf{\Psi}})^T\right) : \left(\nabla\delta\mathbf{u} + (\nabla\delta\mathbf{u})^T\right) + \left(\nabla\tilde{\mathbf{\Psi}} + (\nabla\tilde{\mathbf{\Psi}})^T\right) : \left(\nabla\mathbf{u} + (\nabla\mathbf{u})^T\right). \tag{A-20}$$

We transform the gradients with respect to parameters α and β, we have

$$\nabla E_{\alpha\, or\, \delta\alpha} = \rho \nabla E_{\lambda\, or\, \delta\lambda} \quad \& \tag{A-21}$$

$$\nabla E_{\beta\, or\, \delta\beta} = -2\rho \nabla E_{\lambda\, or\, \delta\lambda} + \rho \nabla E_{\mu\, or\, \delta\mu}. \tag{A-22}$$

REFERENCES

Alkhalifah, T., 2015, Scattering-angle based filtering of the waveform inversion gradients: Geophysical Journal International, **200**, 363–373.

Alkhalifah, T., and Z. Wu, 2016, The natural combination of full and image-based waveform inversion: Geophysical Prospecting, **64**, 19–30.

Berkhout, A. J., 2012, Combining full wavefield migration and full waveform inversion, a glance into the future of seismic imaging: GEOPHYSICS, **77**, S43–S50.

Biondi, B., and A. Almomin, 2014, Simultaneous inversion of full data bandwidth by tomographic full-waveform inversion: Geophysics, **79**, WA129–WA140.

Biondi, B., and W. Symes, 2004, Angle domain common image gathers for migration velocity analysis by wavefield continuation imaging: Geophysics, **69**, 1283–1298.

Brossier, R., S. Operto, and J. Virieux, 2015, Velocity model building from seismic reflection data by full-waveform inversion: Geophysical Prospecting, **63**, 354–367.

Choi, Y., and T. Alkhalifah, 2012, Application of multi-source waveform inversion to marine streamer data using the global correlation norm: Geophysical Prospecting, **60**, 748–758.

———, 2015, Unwrapped phase inversion with an exponential damping: Geophysics, **80**, R251–R264.

Claerbout, J. F., 1985, Imaging the earth's interior: Blackwell Scientific Publications, Inc.

Clément, F., G. Chavent, and S. Gómez, 2001, Migrationbased traveltime waveform inversion of 2-d simple structures: A synthetic example: GEOPHYSICS, **66**, 845–860.

Crase, E., A. Picat, M. Noble, J. McDonalds, and A. Tarantola, 1990, Robust elastic nonlinear waveform inversion: Application to real data: Geophysics, **55**, 527–538.

Duan, Y., A. Guitton, and P. Sava, 2017, Elastic least-squares reverse time migration: GEOPHYSICS, **82**, S315–S325.

Duan, Y., and P. Sava, 2015, Scalar imaging condition for elastic reverse time migration: GEOPHYSICS, **80**, S127–S136.

Guitton, A., and T. Alkhalifah, 2016, Full-waveform inversion in an anisotropic elastic earth - can we isolate the role of density and shear wave velocity?: 78th EAGE Conference and Exhibition 2016.

Hou, J., and W. W. Symes, 2015, An approximate inverse to the extended born modeling operator: GEOPHYSICS, **80**, R331–R349.

Lailly, P., 1983, The seismic inverse problem as a sequence of before stack migrations: Conference on inverse scattering: theory and application, 206–220.

Ma, Y., and D. Hale, 2013, Wave-equation reflection traveltime inversion with dynamic warping and full-waveform inversion: GEOPHYSICS, **78**, R223–R233.

Mora, P., 1987, Nonlinear two-dimensional elastic inversion of multioffset seismic data: Geophysics, **52**, 1211–1228.

———, 1989, *in* Inversion=migration+tomography: Springer Berlin Heidelberg, 78–101.

Oh, J.-W., and T. Alkhalifah, 2016, The scattering potential of partial derivative wavefields in 3-d elastic orthorhombic media: an inversion prospective: Geophysical Journal International, **206**, 1740–1760.

Operto, S., Y. Gholami, R. Brossier, L. Métivier, V. Prieux, A. Ribodetti, and J. Virieux, 2013, A guided tour of multi-parameter full waveform inversion with multi-component data: from theory to practice: The Leading Edge, **32**, 1040–1054.

Plessix, R., Y. D. Roeck, and G. Chavent, 1995, Automatic and simultaneous migration velocity analysis and waveform inversion of real data using a mbtt/wkb j formulation: SEG Technical Program Expanded Abstracts 1995, 1099–1102.

Plessix, R.-E., 2006, A review of the adjoint-state method for computing the gradient of a

functional with geophysical applications: Geophysical Journal International, **167**, 495–503.

Prieux, V., R. Brossier, S. Operto, and J. Virieux, 2013, Multiparameter full waveform inversion of multicomponent ocean-bottom-cable data from the valhall field. part 1: imaging compressional wave speed, density and attenuation: Geophysical Journal International, **194**, 1640–1664.

Rocha, D., N. Tanushev, and P. Sava, 2017, Anisotropic elastic wavefield imaging using the energy norm: GEOPHYSICS, **82**, S225–S234.

Sava, P. C., B. Biondi, and J. Etgen, 2005, Wave-equation migration velocity analysis by focusing diffractions and reflections: Geophysics, **70**, U19–U27.

Staal, X., and D. Verschuur, 2013, Joint migration inversion, imaging including all multiples with automatic velocity update: 75th EAGE Conference & Exhibition incorporating SPE EUROPEC 2013.

Symes, W. W., 2008, Migration velocity analysis and waveform inversion: Geophysical Prospecting, **56**, 765–790.

Symes, W. W., and M. Kern, 1994, Inversion of reflection seismograms by differential semblance analysis: algorithm structure and synthetic examples1: Geophysical Prospecting, **42**, 565–614.

Szydlik, T., P. Smith, S. Way, L. Aamodt, and C. Friedrich, 2007, 3d pp/ps prestack depth migration on the volve field: First Break, **25**, 43–47.

Tarantola, A., 1984, Inversion of seismic reflection data in the acoustic approximation: Geophysics, **49**, 1259–1266.

———, 1986, A strategy for nonlinear elastic inversion of seismic reflection data: Geophysics, **51**, 1893–1903.

Virieux, J., and S. Operto, 2009, An overview of full-waveform inversion in exploration geophysics: GEOPHYSICS, **74**, WCC1–WCC26.

Wang, S., F. Chen, H. Zhang, and Y. Shen, 2013, Reflection-based full waveform inversion (rfwi) in the frequency domain: 83rd Annual International Meeting, SEG, Expanded Abstracts, 877–881.

Wang, T. F., J. B. Cheng, and C. L. Wang, 2015, Elastic wave mode decoupling for full waveform inversion: 77th Conference & Exhibition, EAGE, Extended Abstracts.

Wu, R.-S., and Y. Zheng, 2014, Non-linear partial derivative and its de wolf approximation for non-linear seismic inversion: Geophysical Journal International, **196**, 1827–1843.

Wu, Z., and T. Alkhalifah, 2014, Full waveform inversion based on the optimized gradient and its spectral implementation: 76th Conference & Exhibition, EAGE, Extended Abstracts.

———, 2015, Simultaneous inversion of the background velocity and the perturbation in full-waveform inversion: Geophysics, **80**, R317–R329.

Xu, S., D. Wang, F. Chen, Y. Zhang, and G. Lambare, 2012, Full waveform inversion for reflected seismic data: 74th Conference & Exhibition incorporating SPE EUROPEC, EAGE, Extended Abstracts.

Yan, J., and P. Sava, 2008, Isotropic angle-domain elastic reverse-time migration: Geophysics, **73**, S229–S239.

Yang, D., X. Shang, A. Malcolm, M. Fehler, and H. Baek, 2015, Image registration guided wavefield tomography for shear-wave velocity model building: GEOPHYSICS, **80**, U35–U46.

Zhou, H., L. Amundsen, and G. Zhang, 2012, Fundamental issues in full waveform inversion: SEG Technical Program Expanded Abstracts 2012, 1–5.

Zhou, W., R. Brossier, S. Operto, and J. Virieux, 2015, Full waveform inversion of diving and reflected waves for velocity model building with impedance inversion based on scale separation: Geophysical Journal International, **202**, 1535–1554.

LIST OF TABLES

LIST OF FIGURES

ERWI without the frequencies lower than 3hz and (d) the inverted S-wave velocity from EFWI.

7 The velocity profile of P-wave (a) and of S-wave in the middle of the model (black: initial; blue: true; red: ERWI result; pink dash: EFWI result). Without the low frequencies, EFWI can only fit the P-wave velocity at the shallow part, while our ERWI achieves good estimates for both P- and S-wave velocities.

8 The true model perturbations $\delta\alpha$ (a) and $\delta\beta$ (b); the inverted $\delta\alpha$ (c) and $\delta\beta$ (d). In getting the true model perturbations, we filter out the wavenumbers below 1 as our optimization of the model perturbations are not to fit the low wavenumebers of the difference between the true and the initial models.

9 The convergence curve. It takes 3 outer loops in our inversion for Marmousi model. In each outer loop, we first execute 20 iterations focused on updating the model perturbations using the L2-norm misfit function, and 10 iterations in updating the backgrounds using the correlation-based misfit function. The jumps in the curve correspond to the normalized starting values of different stages of optimization.

10 (a) The tomography P-wave velocity and (b) the initial P-wave velocity; (c) the tomography S-wave velocity and (d) the initial S-wave velocity. The initial models smear out most of the structures including the chalk layer and the subchalk low velocity zone.

11 The vertical component of the observed data between 2 and 6 Hz (left-hand side) and predicted data after second stage (right-hand side) (a); the vertical component of the observed data between 2 and 8 Hz (left-hand side) and predicted data after third stage (right-hand side) (b). The predicted data match well with the main reflection events. We attribute the unmatched events to two possible factors: the missing PS and PP events in the provided data and the internal multiples that appear as additional events in our

prediction, but have been suppressed in the provided data.

12 The inverted background P-wave velocity (a) with the inverted perturbation added to it (b); the inverted background S-wave velocity (c) with the inverted perturbation added to it (d).

13 The reverse time migration (RTM) calculated by initial smoothed tomography model (a) and by our inverted P-wave velocity (b). We apply acoustic RTM with vertical component of the data between 2 and 30 Hz in order to show a high-resolution result and more details.

14 The PP image gathers (a) calculated by elastic RTM using the smoothed tomography model and (b) calculated using our ERWI model. The horizontal position of gather ranges from 4.06 km to 7.69 km. The improved areas are indicated by the yellow arrows.

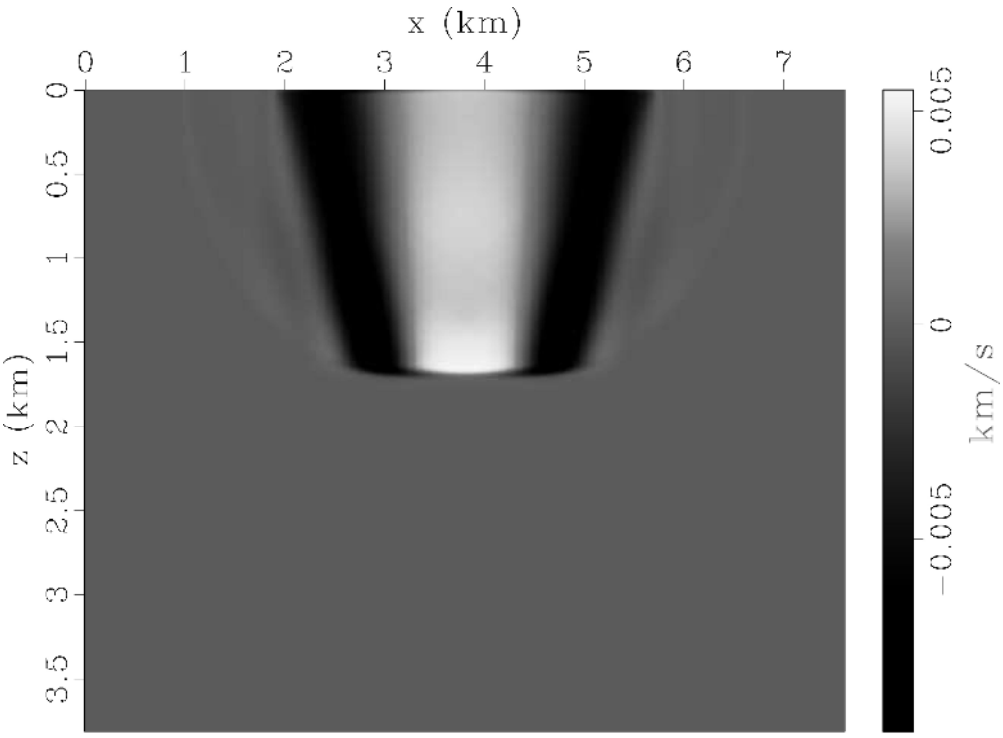

Figure 1 (a)

223x164mm (300 x 300 DPI)

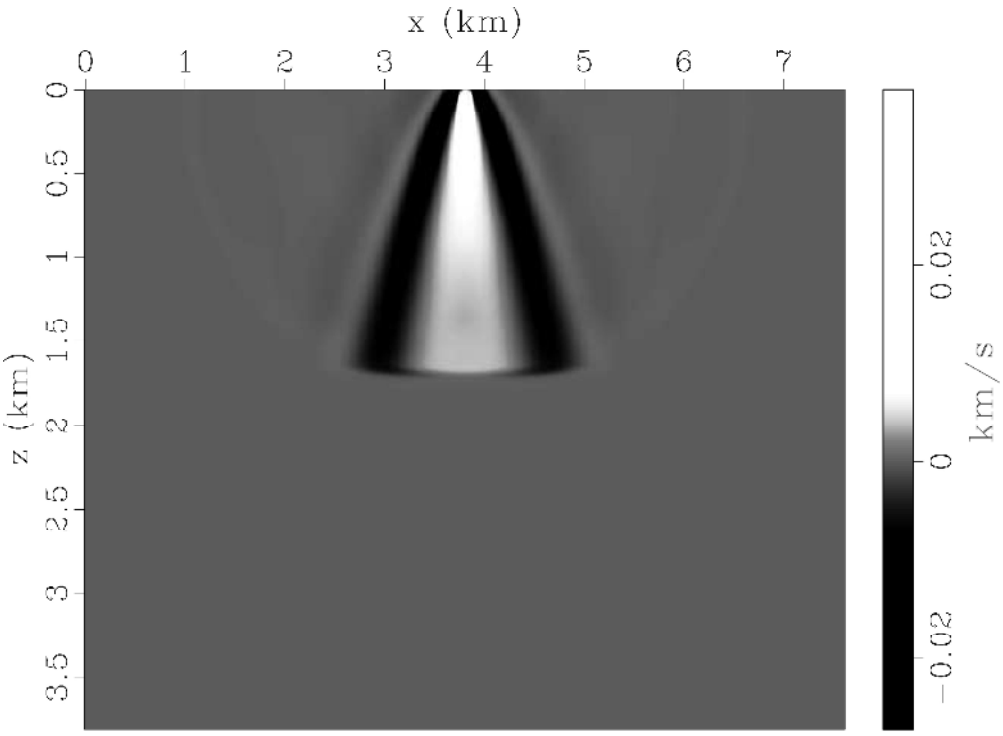

Figure 1 (b)

223x163mm (300 x 300 DPI)

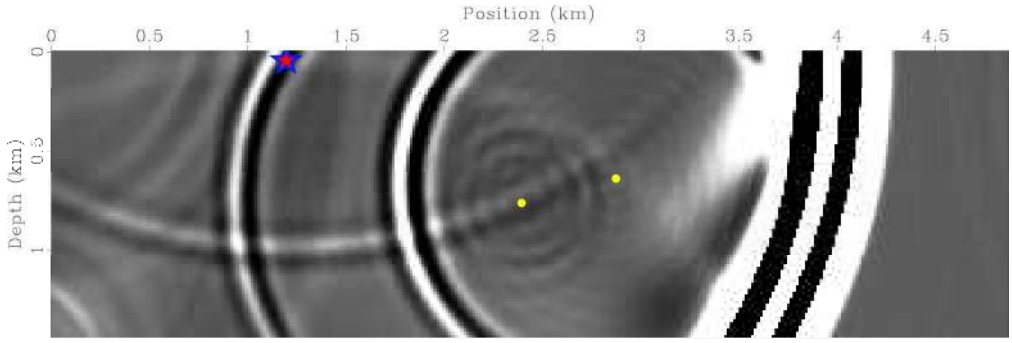

Figure 2 (a)

226x75mm (300 x 300 DPI)

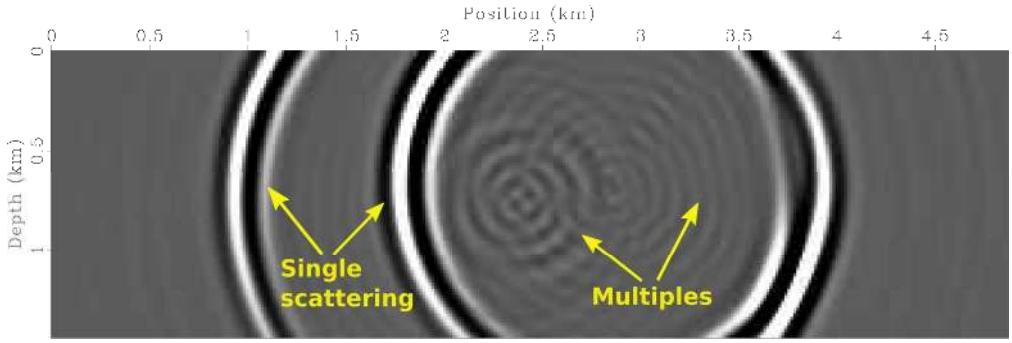

Figure 2 (b)

226x75mm (300 x 300 DPI)

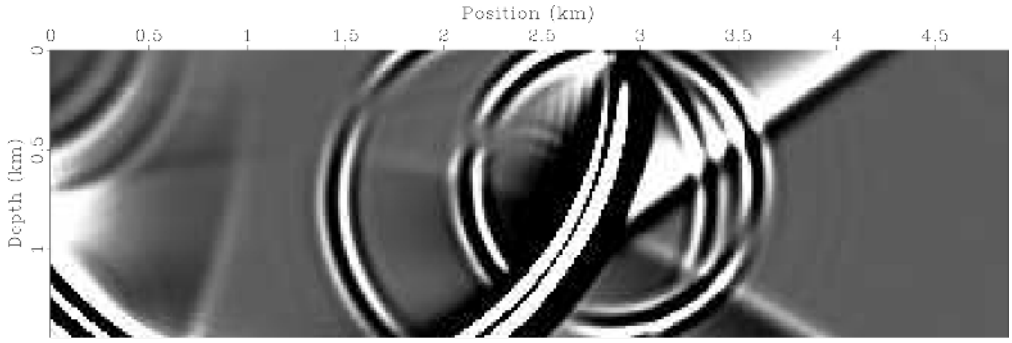

Figure 2 (c)

226x75mm (300 x 300 DPI)

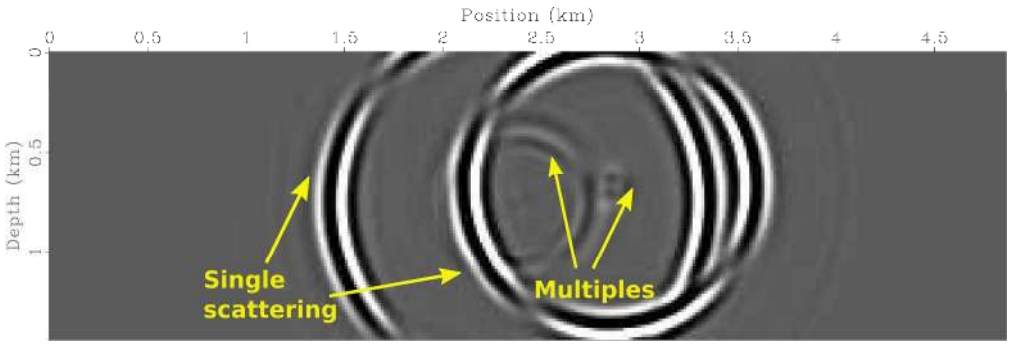

Figure 2 (d)

225x75mm (300 x 300 DPI)

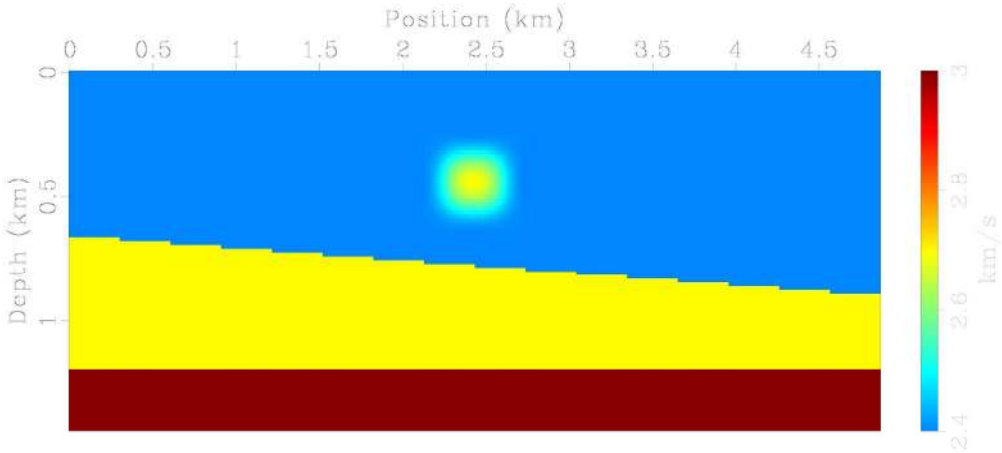

Figure 3 (a)

242x109mm (300 x 300 DPI)

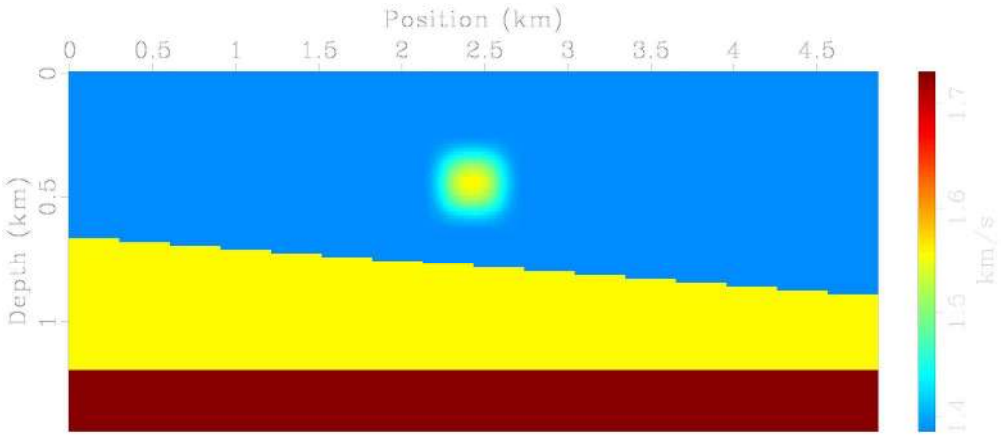

Figure 3 (b)

233x101mm (300 x 300 DPI)

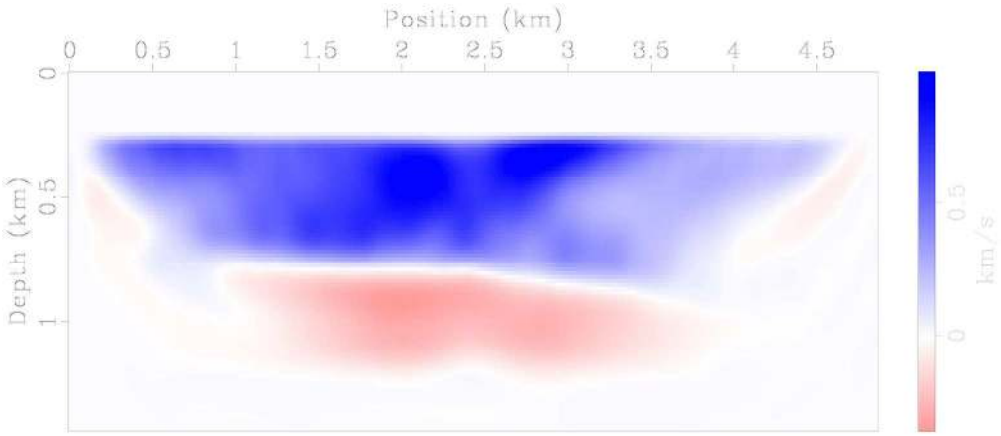

Figure 3 (c)

233x101mm (300 x 300 DPI)

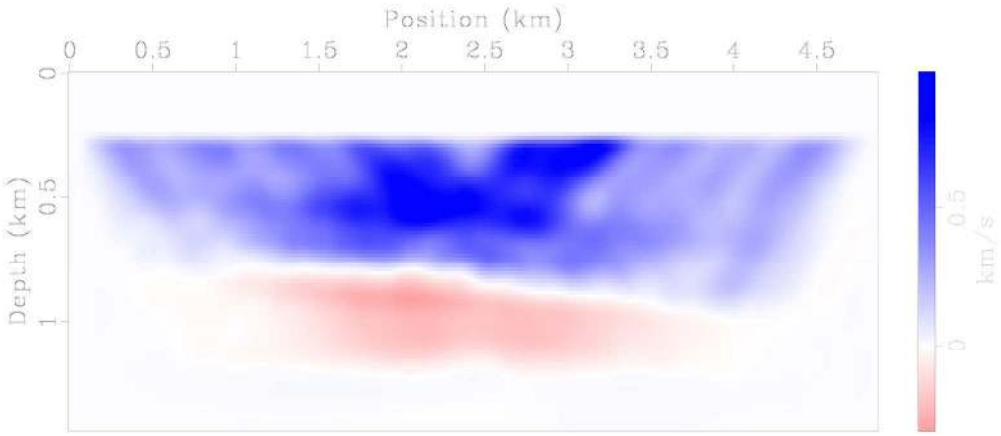

Figure 3 (d)

233x101mm (300 x 300 DPI)

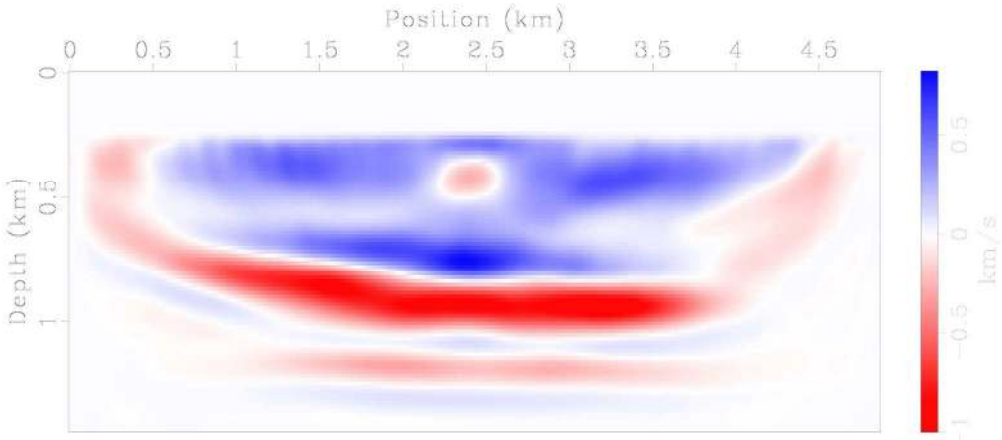

Figure 3 (e)

241x107mm (300 x 300 DPI)

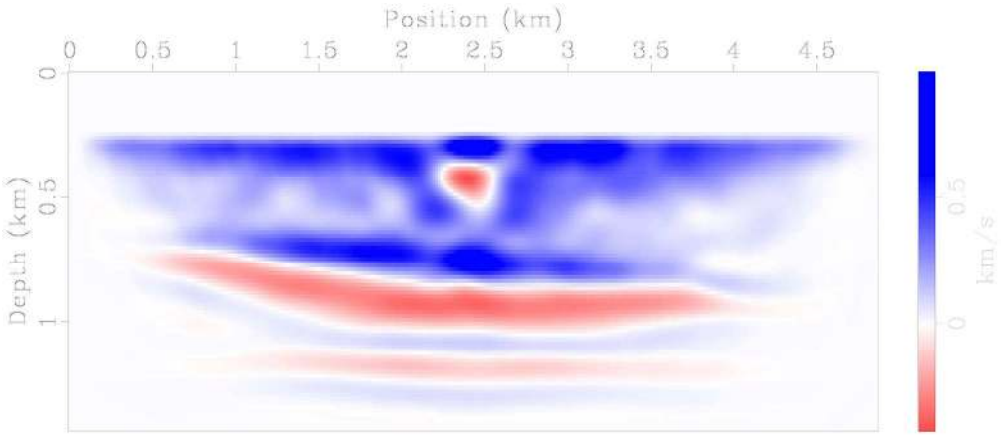

Figure 3 (f)

233x101mm (300 x 300 DPI)

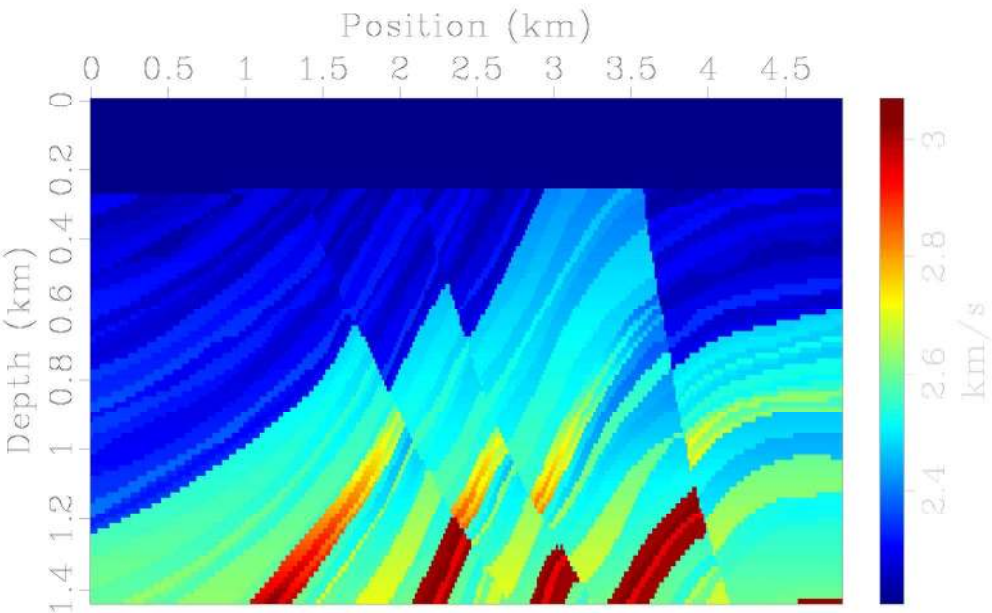

Figure 4 (a)

236x144mm (300 x 300 DPI)

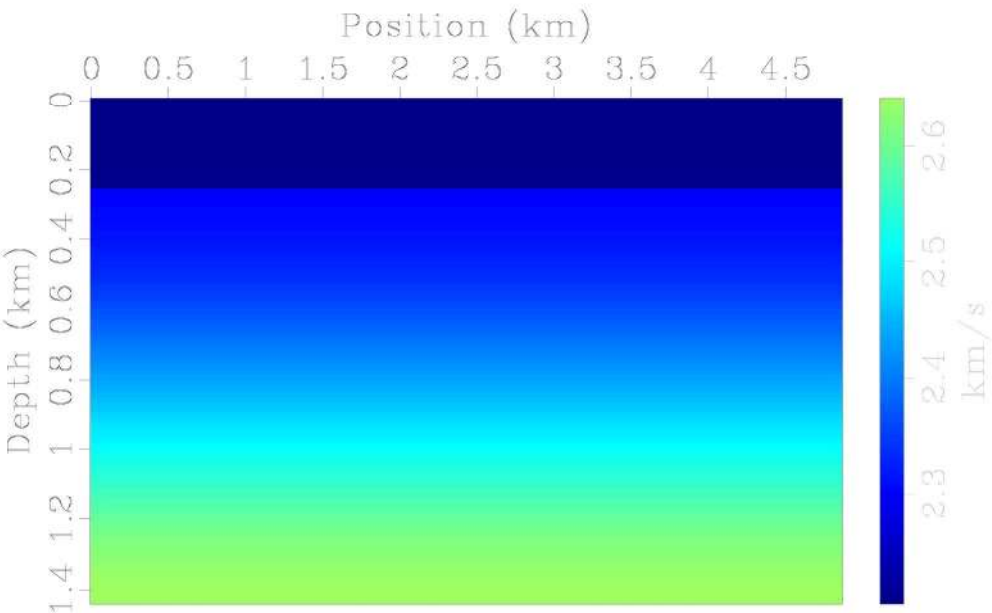

Figure 4 (b)

236x144mm (300 x 300 DPI)

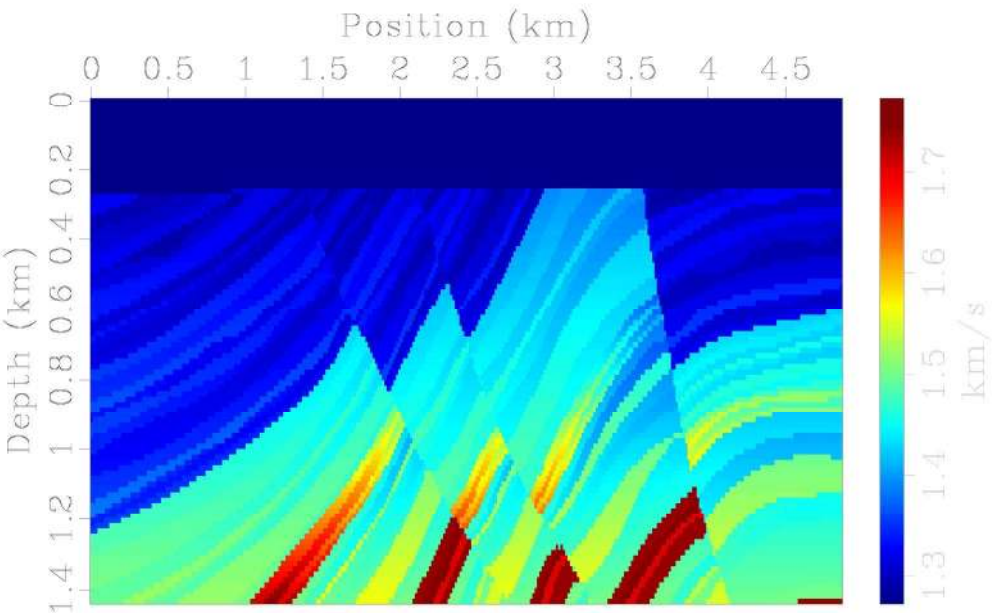

Figure 4 (c)

236x144mm (300 x 300 DPI)

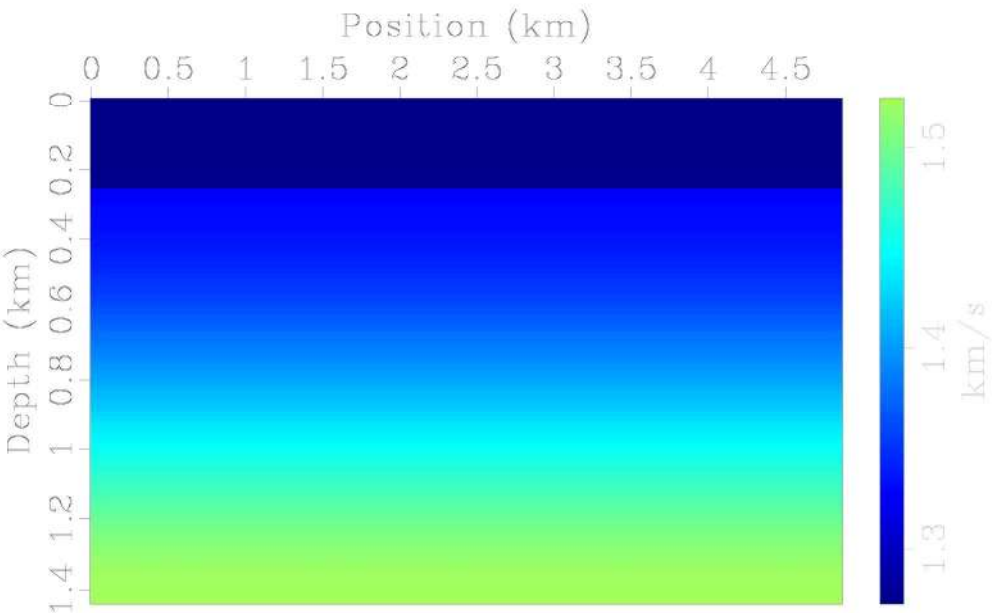

Figure 4 (d)

236x144mm (300 x 300 DPI)

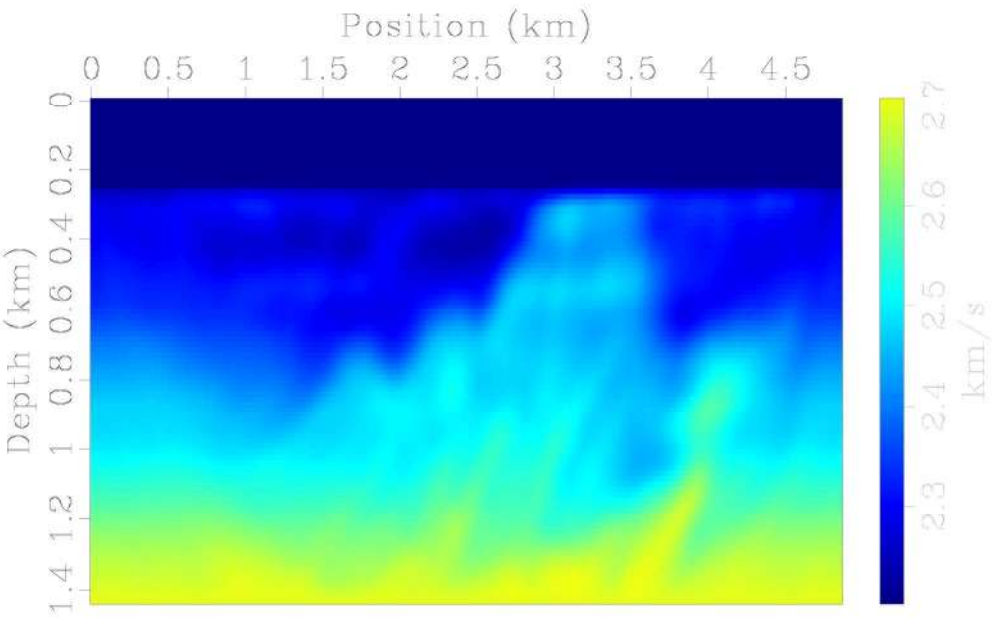

Figure 5 (a)

236x144mm (300 x 300 DPI)

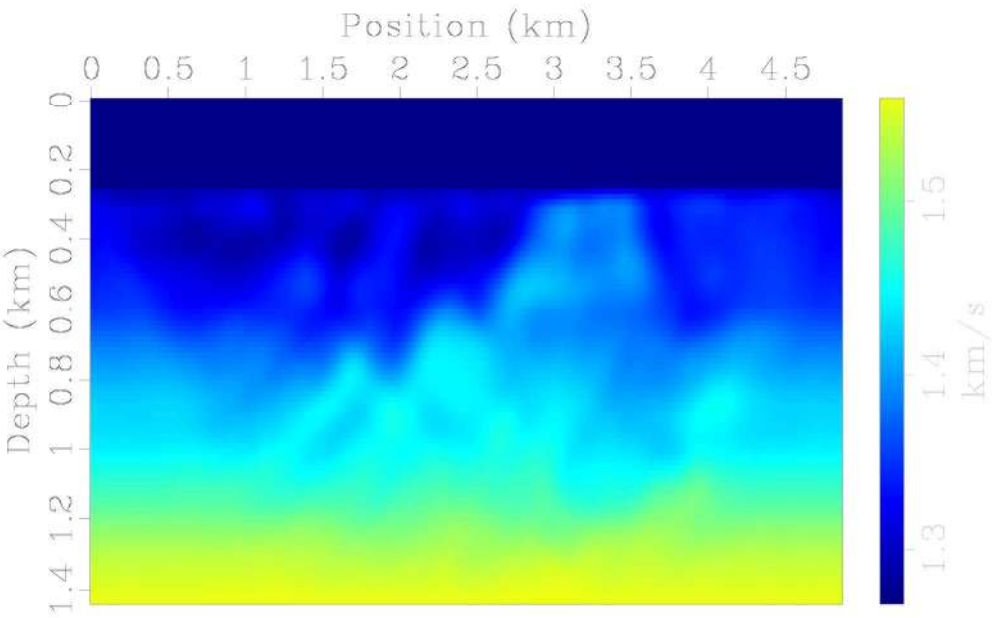

Figure 5 (b)

236x144mm (300 x 300 DPI)

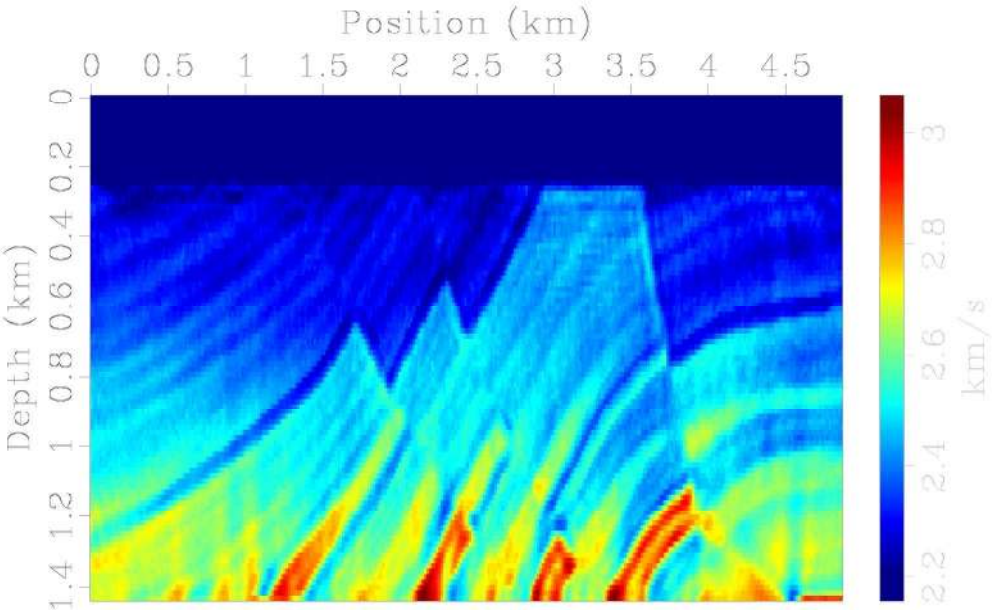

Figure 5 (c)

236x144mm (300 x 300 DPI)

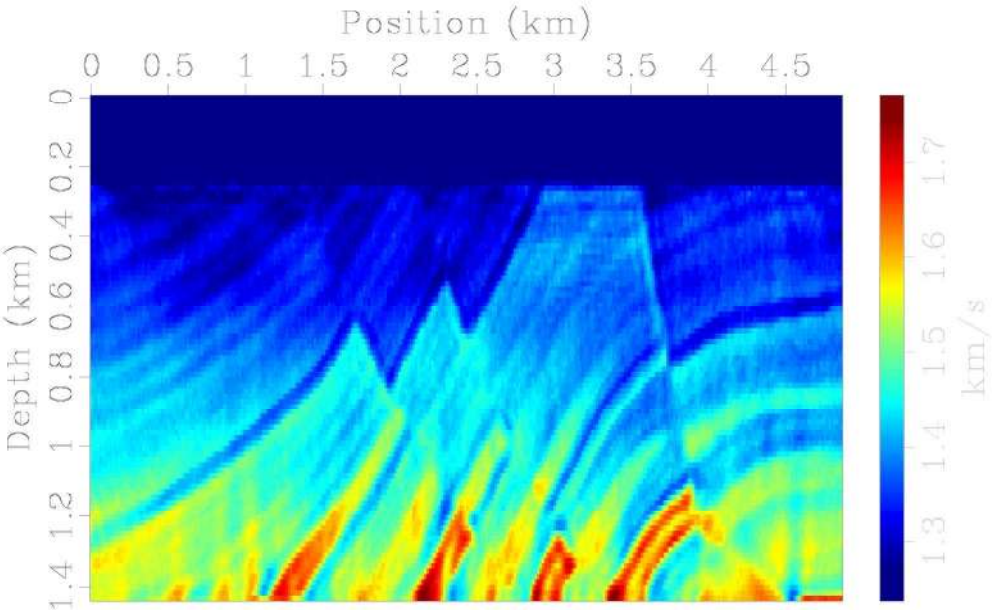

Figure 5 (d)

236x144mm (300 x 300 DPI)

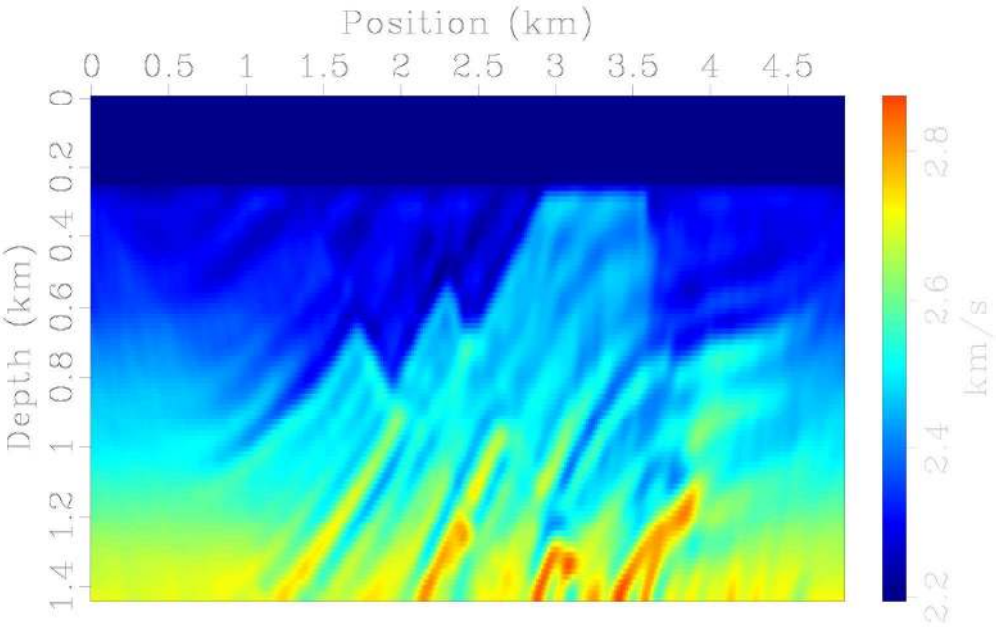

Figure 5 (e)

241x151mm (300 x 300 DPI)

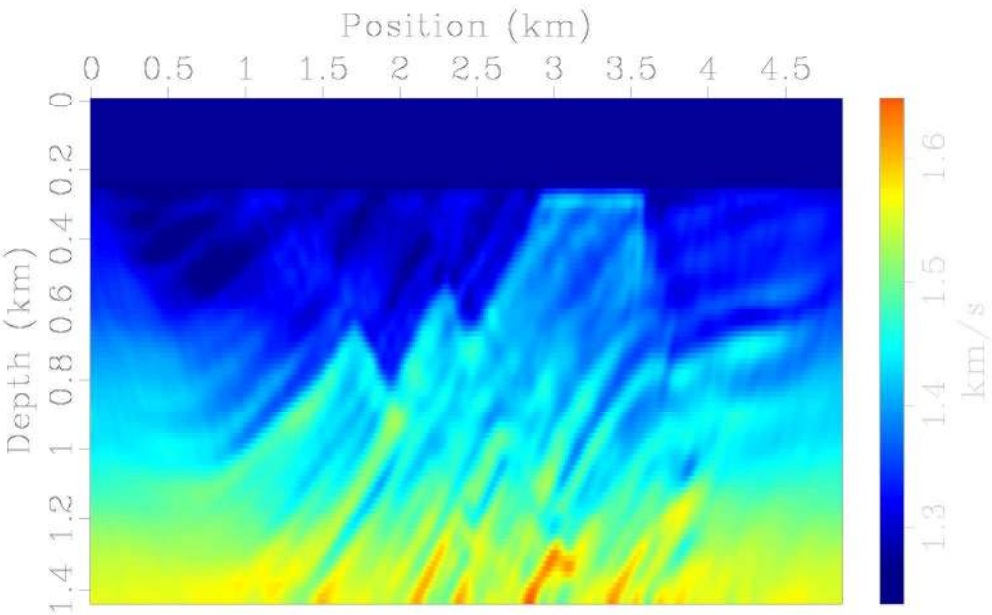

Figure 5 (f)

236x144mm (300 x 300 DPI)

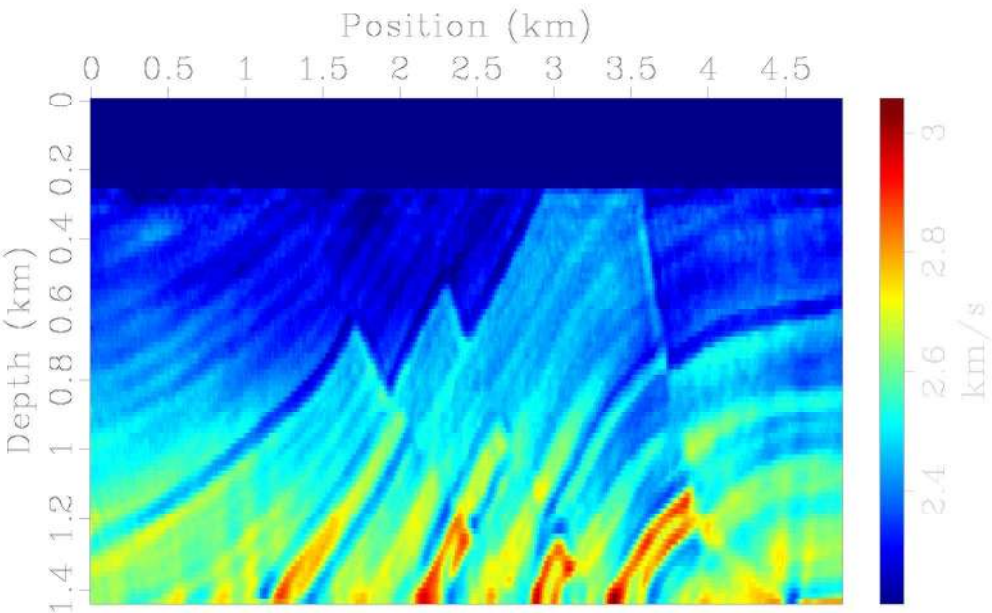

Figure 6 (a)

236x144mm (300 x 300 DPI)

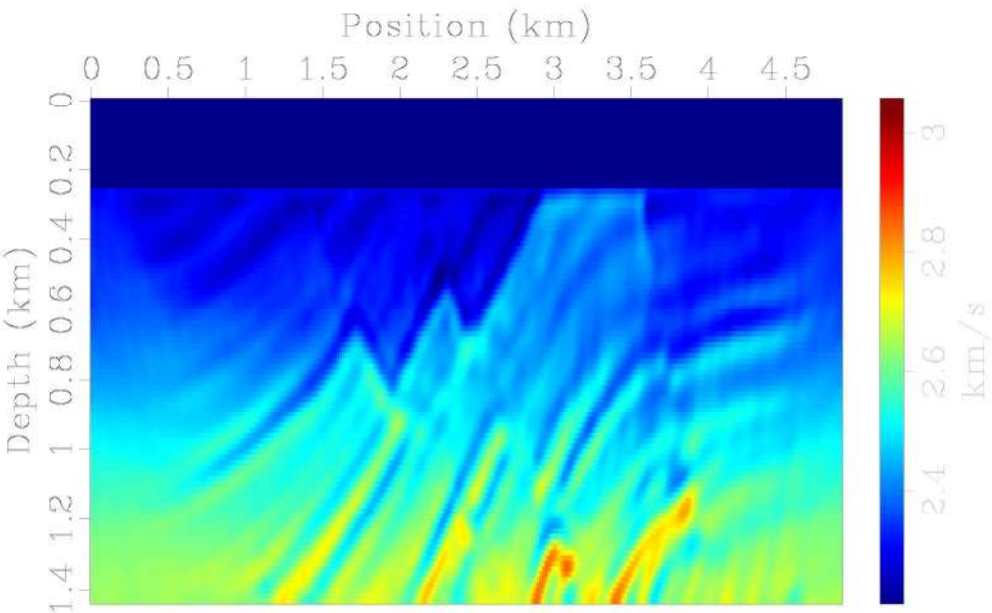

Figure 6 (b)

236x144mm (300 x 300 DPI)

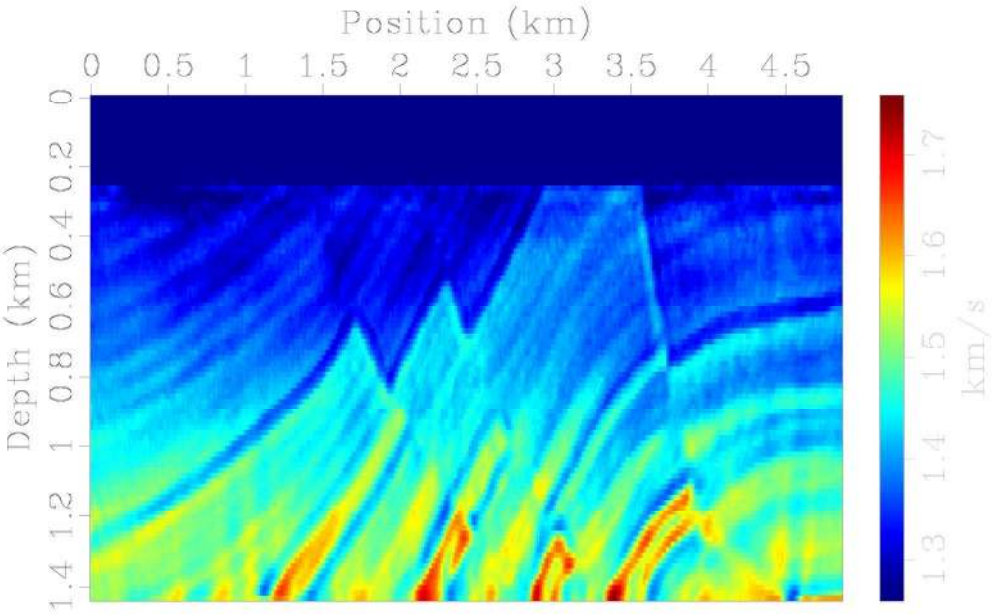

Figure 6 (c)

236x144mm (300 x 300 DPI)

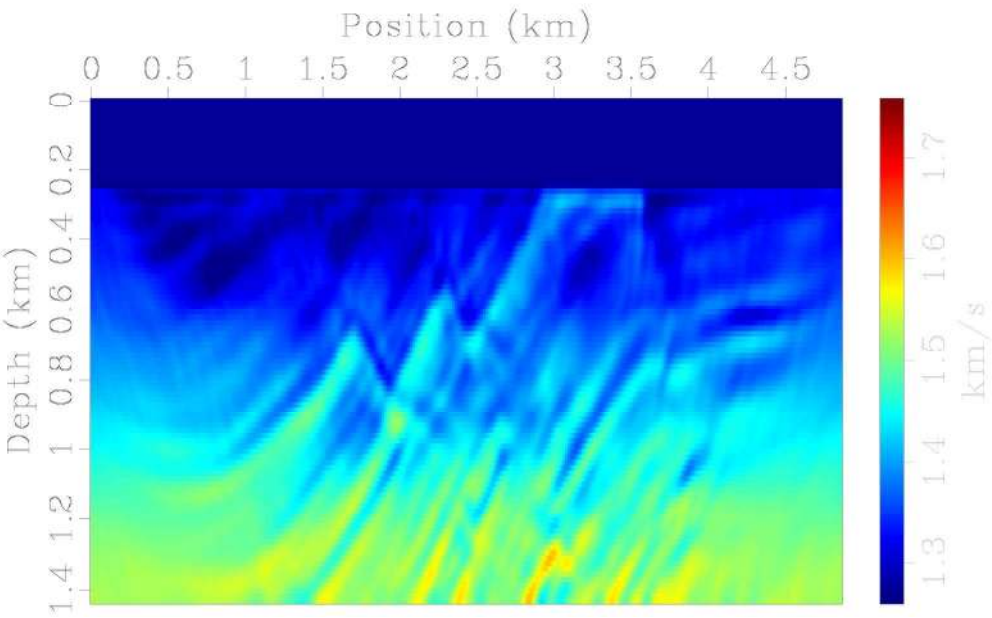

Figure 6 (d)

236x144mm (300 x 300 DPI)

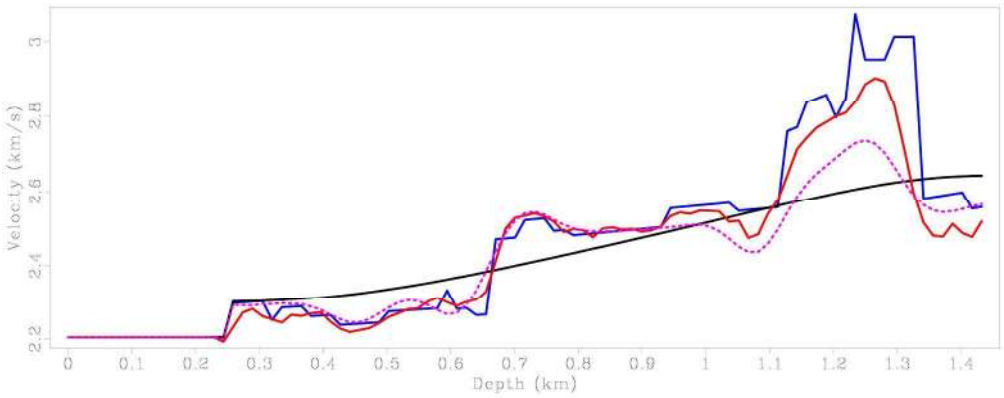

Figure 7 (a)

225x88mm (300 x 300 DPI)

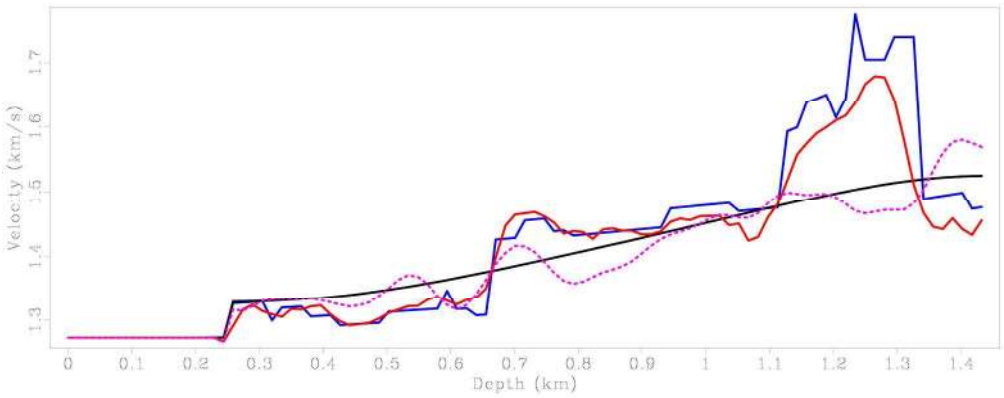

Figure 7 (b)

225x88mm (300 x 300 DPI)

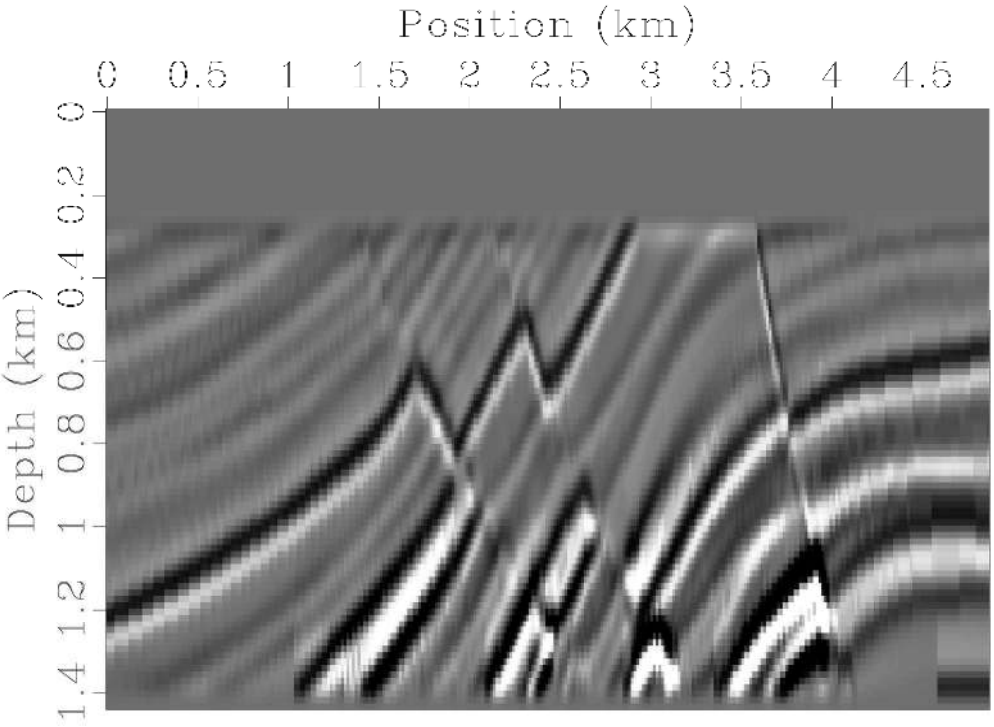

Figure 8 (a)

236x171mm (300 x 300 DPI)

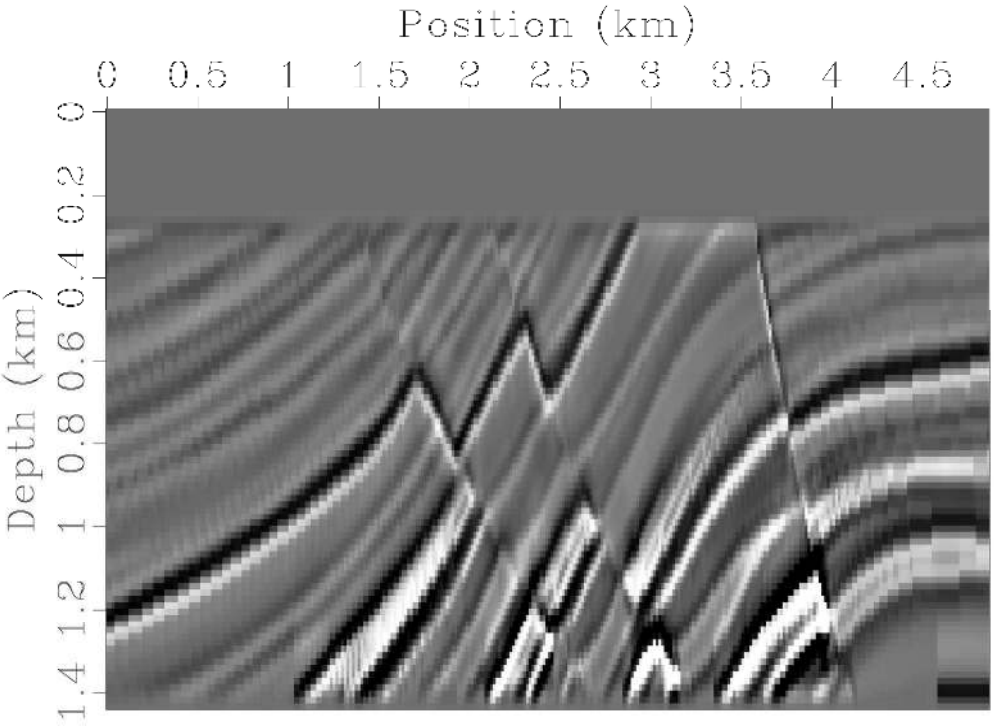

Figure 8 (b)

236x171mm (300 x 300 DPI)

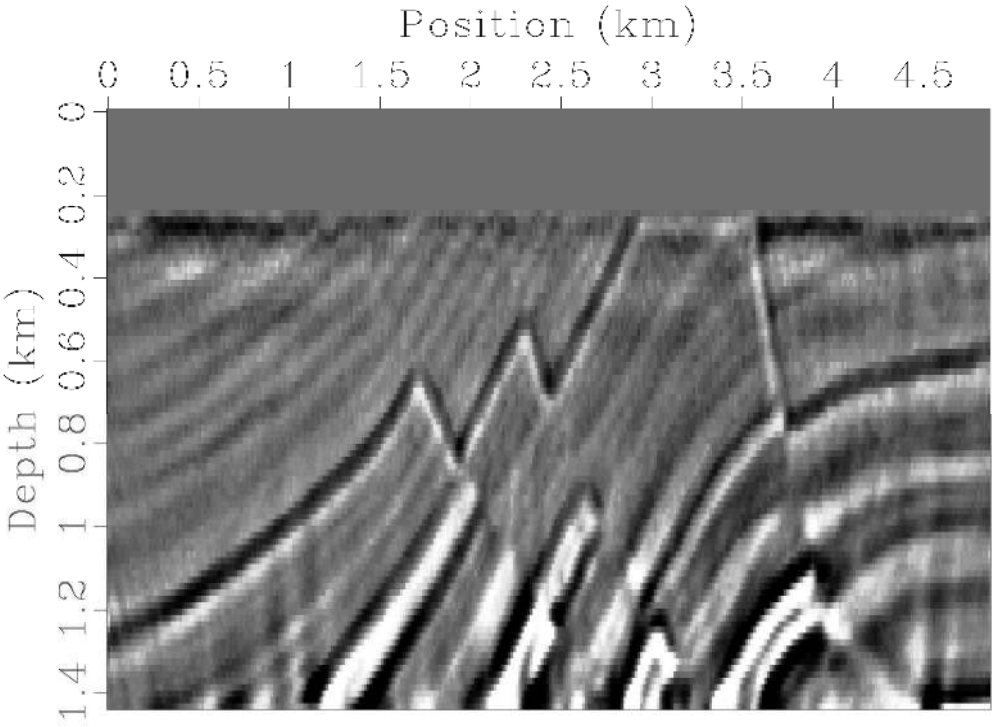

Figure 8 (c)

236x171mm (300 x 300 DPI)

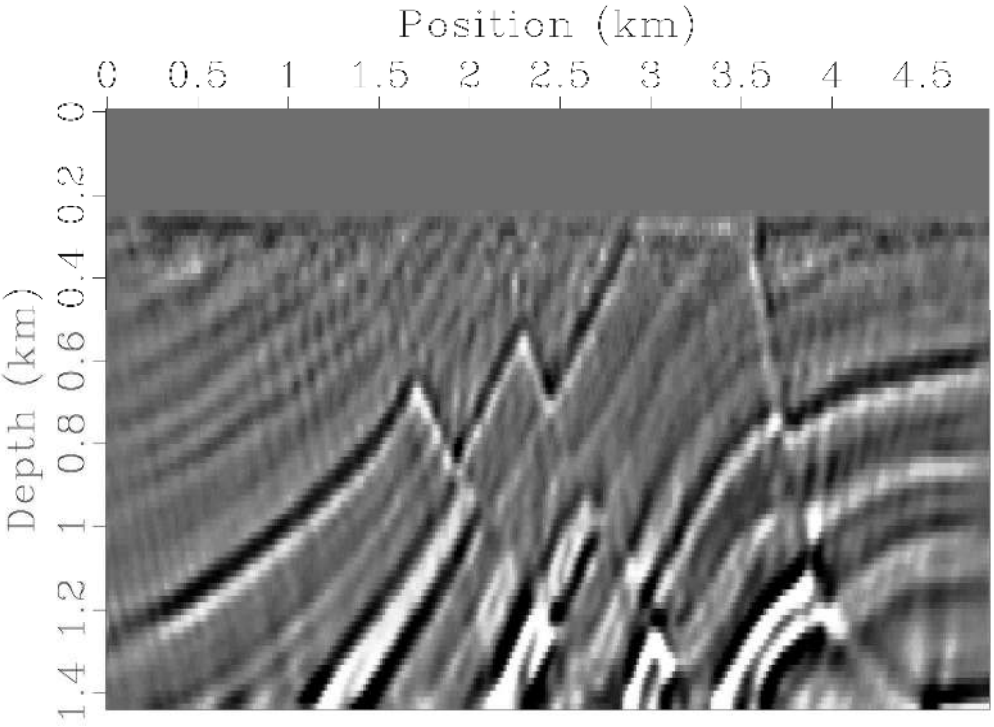

Figure 8 (d)

236x171mm (300 x 300 DPI)

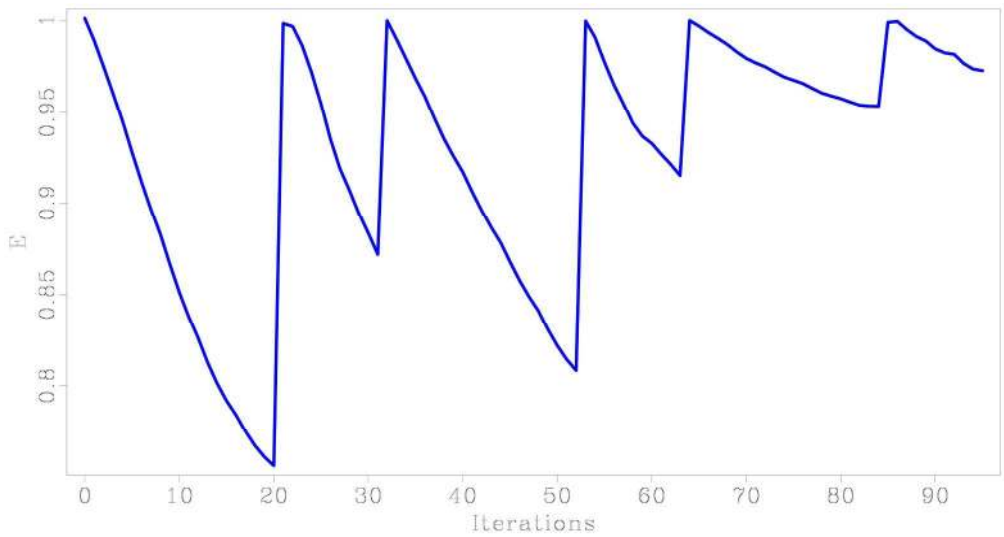

Figure 9

223x118mm (300 x 300 DPI)

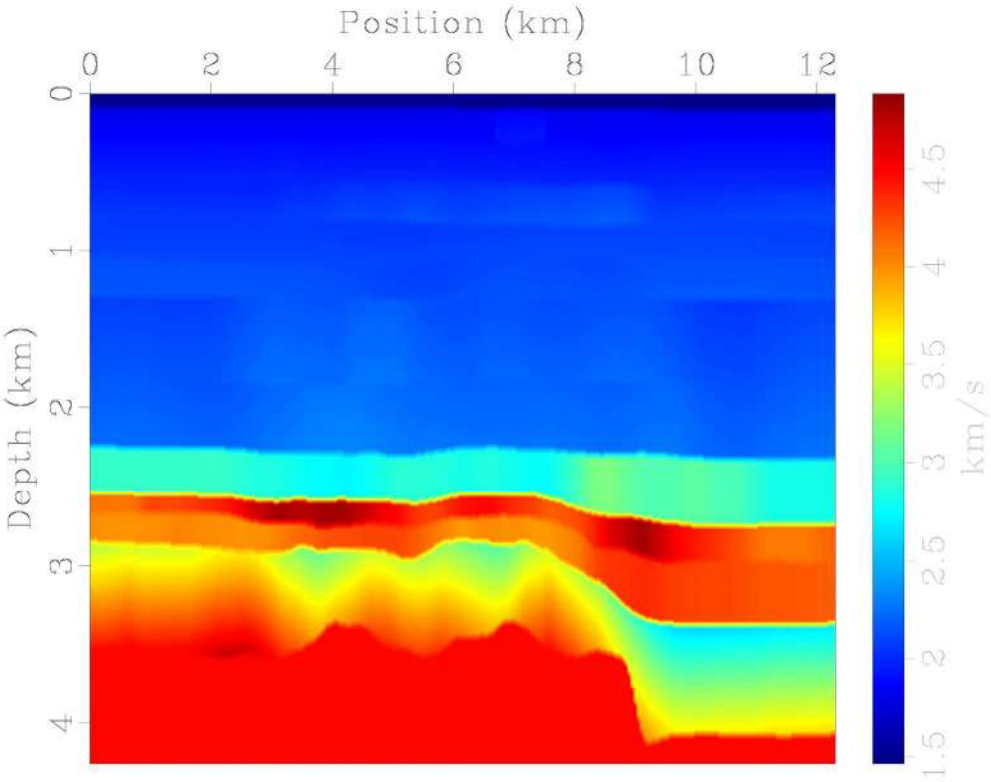

Figure 10 (a)

228x179mm (300 x 300 DPI)

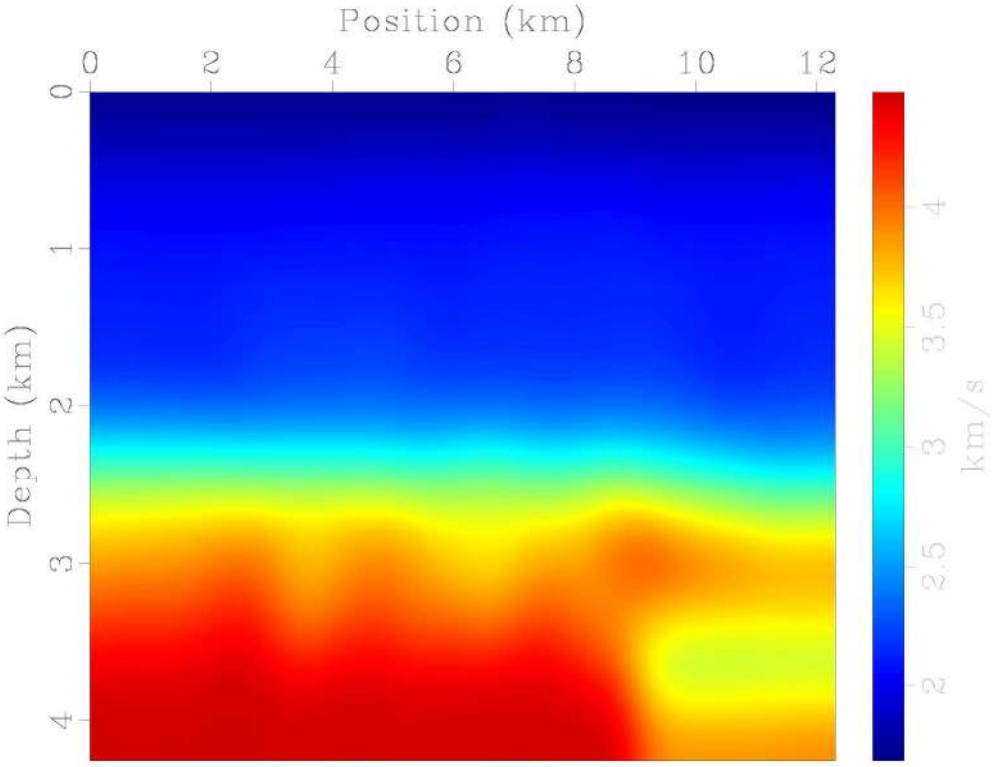

Figure 10 (b)

225x173mm (300 x 300 DPI)

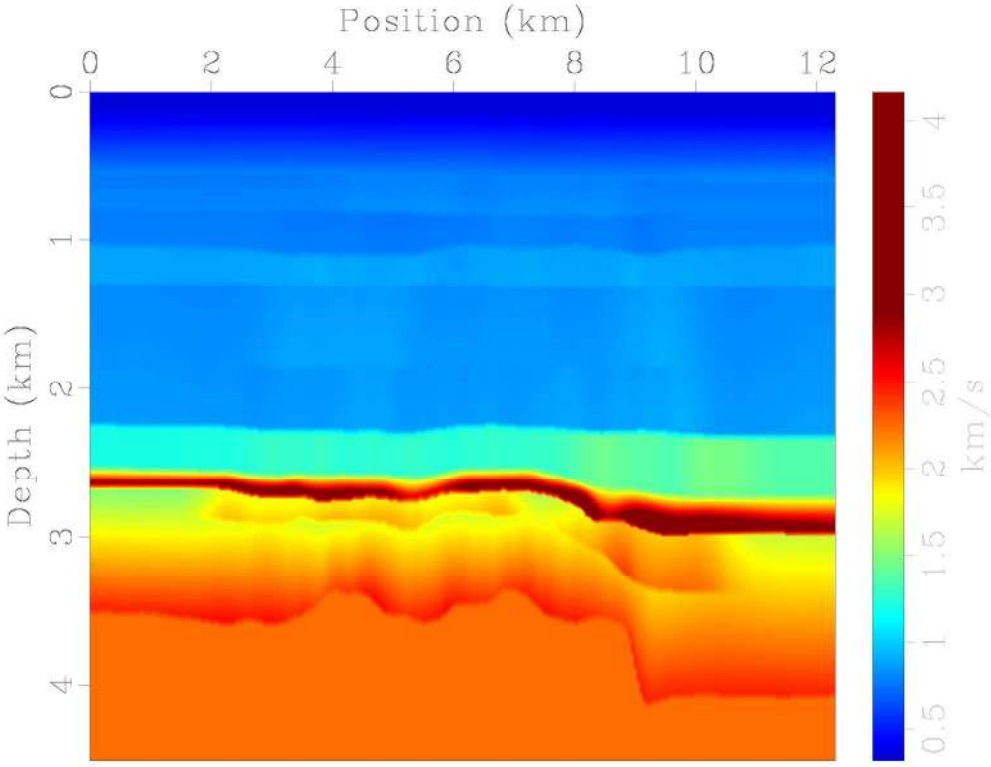

Figure 10 (c)

225x173mm (300 x 300 DPI)

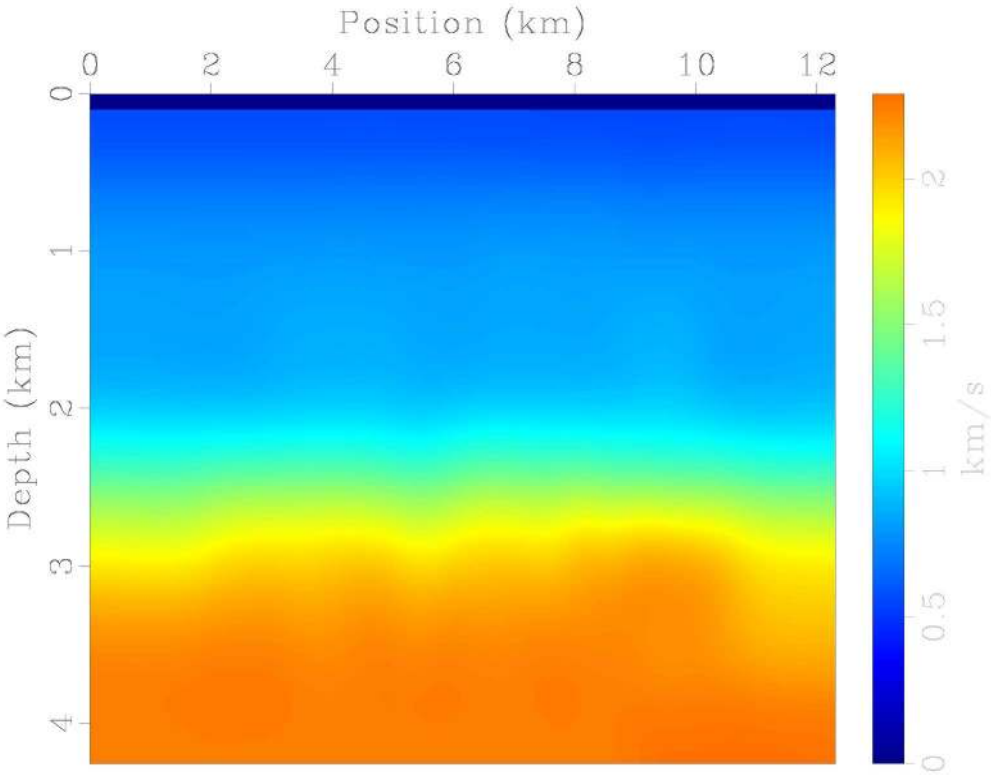

Figure 10 (d)

227x177mm (300 x 300 DPI)

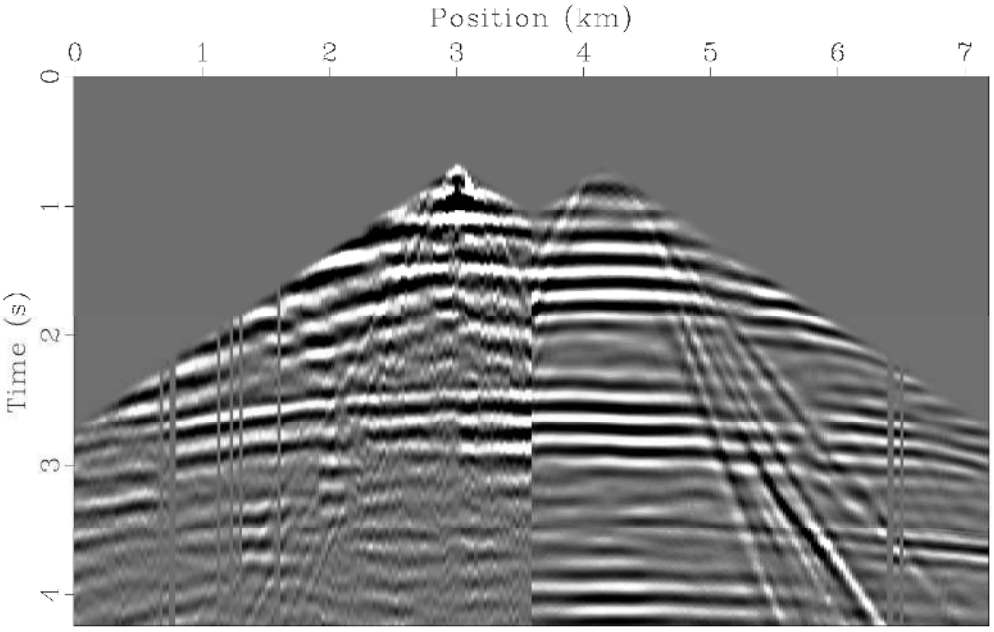

Figure 11 (a)

225x142mm (300 x 300 DPI)

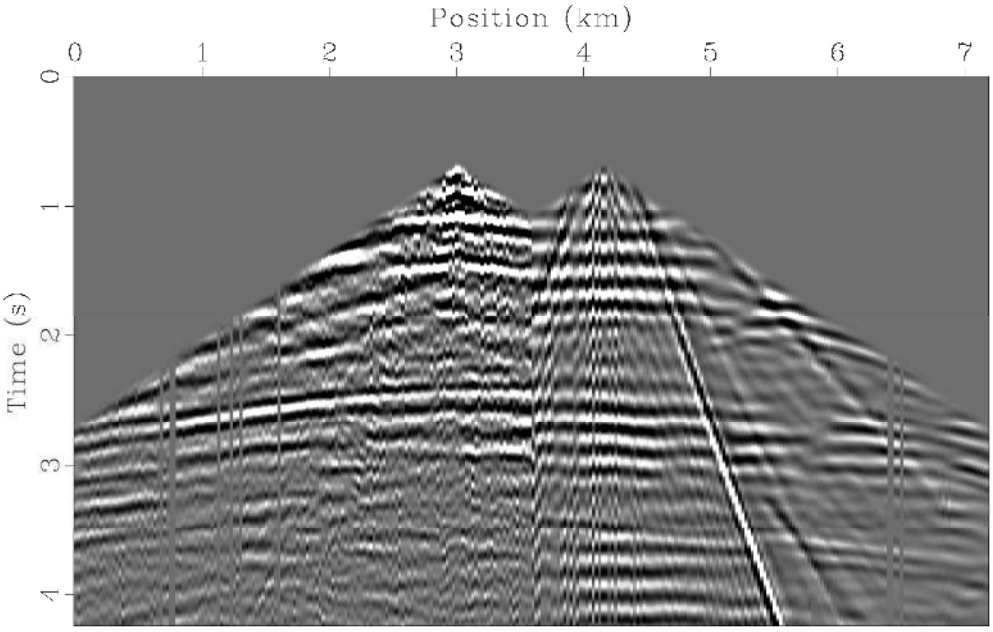

Figure 11 (b)

225x142mm (300 x 300 DPI)

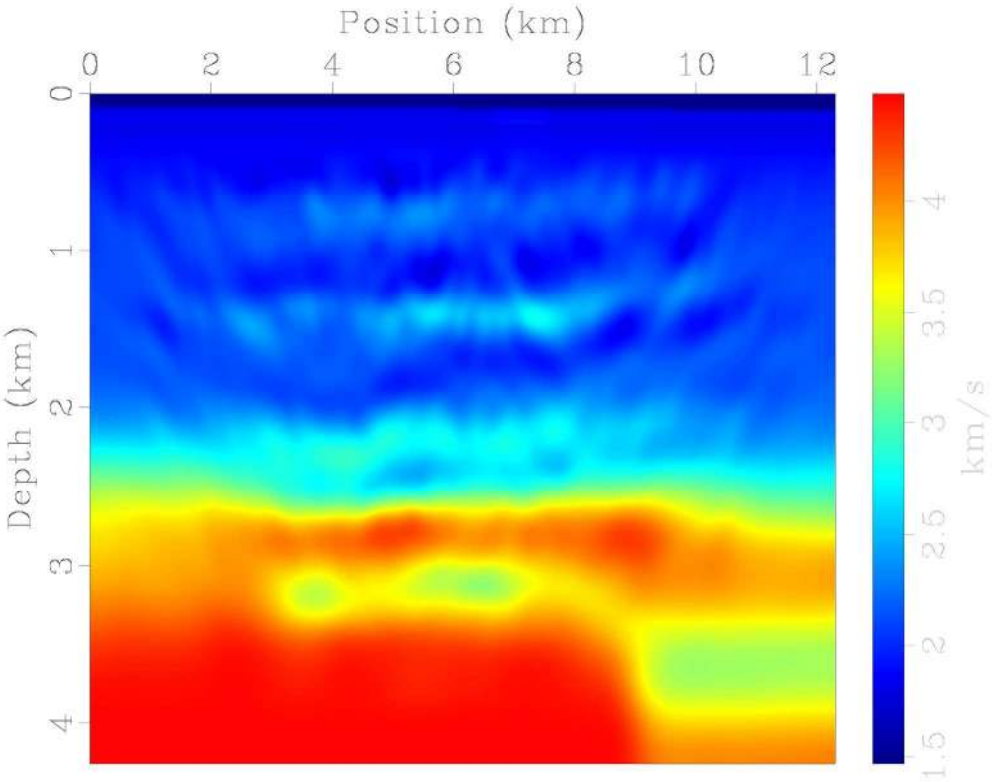

Figure 12 (a)

228x179mm (300 x 300 DPI)

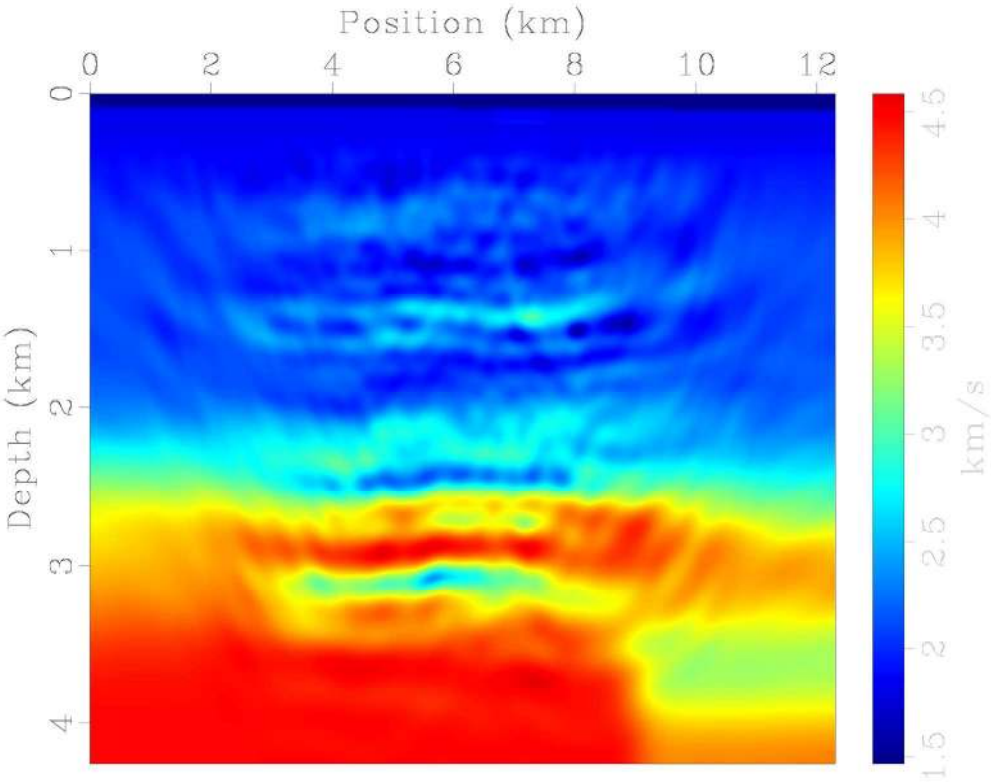

Figure 12 (b)

228x179mm (300 x 300 DPI)

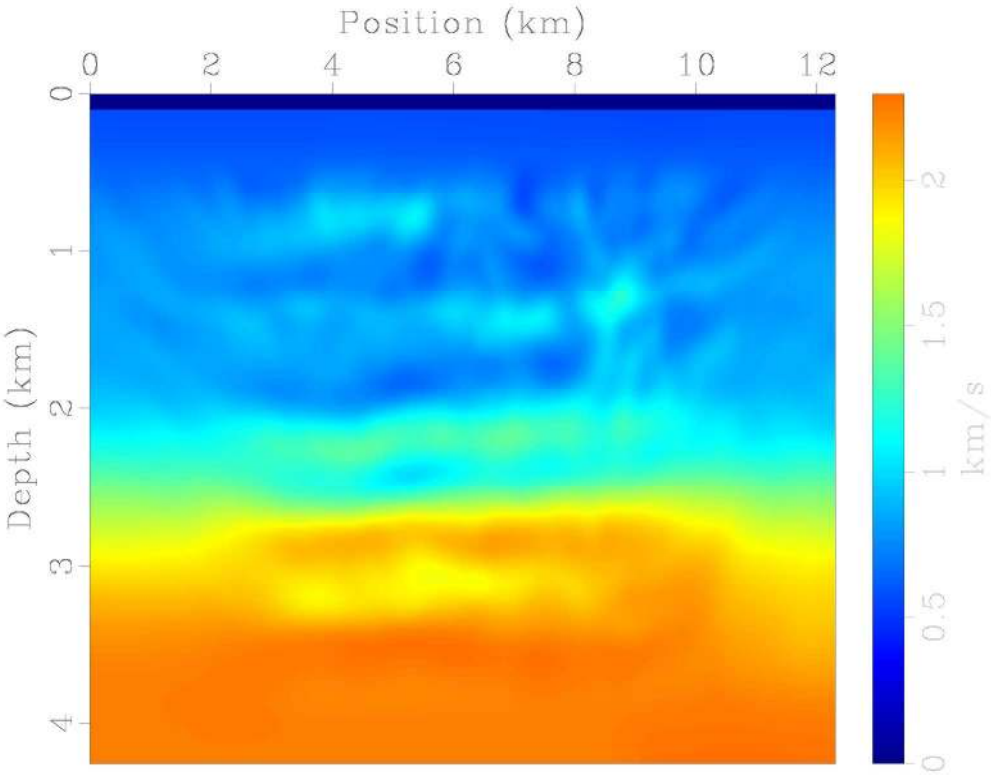

Figure 12 (c)

227x177mm (300 x 300 DPI)

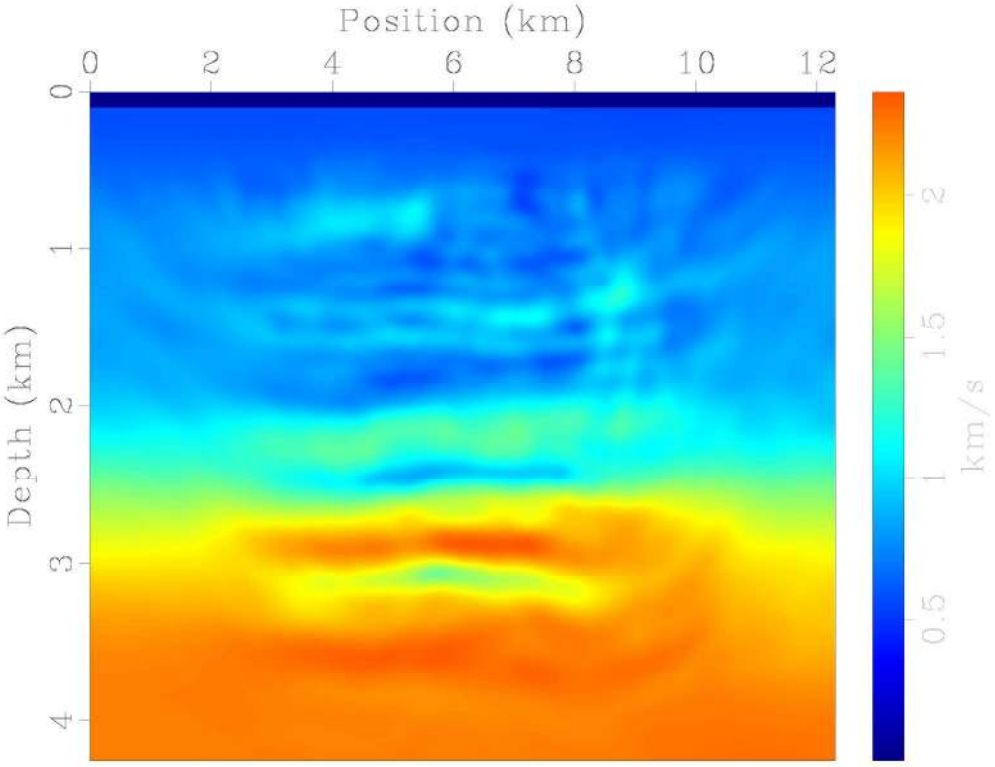

Figure 12 (d)

225x173mm (300 x 300 DPI)

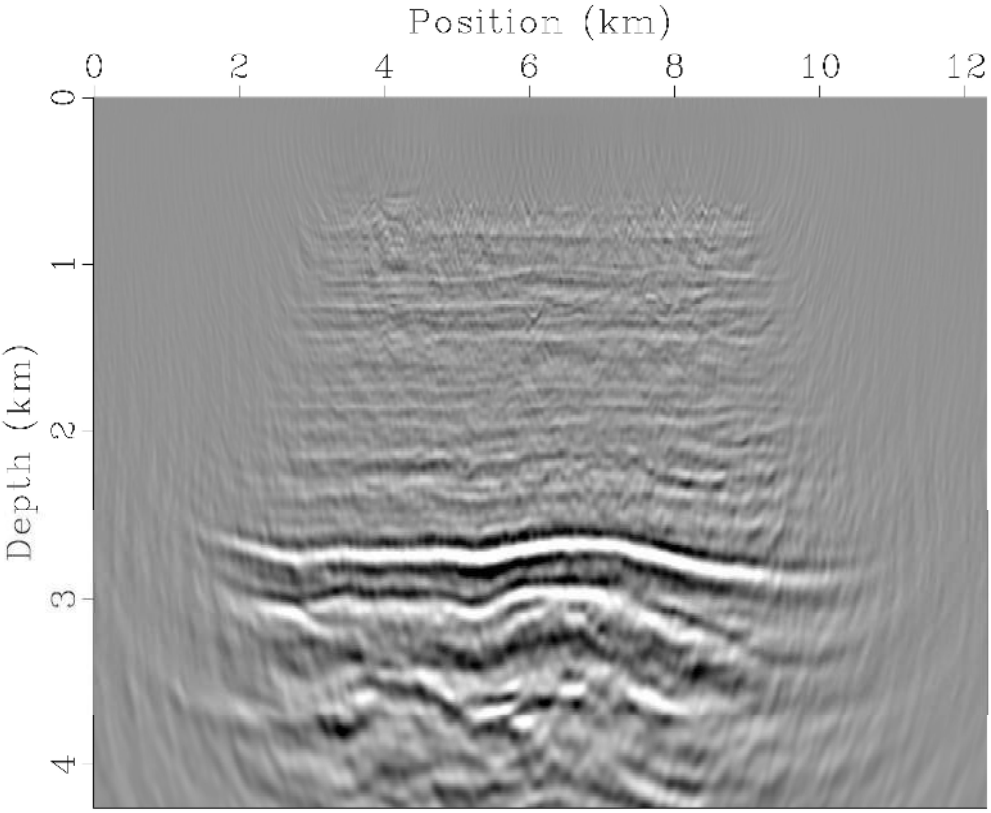

Figure 13 (a)

225x185mm (300 x 300 DPI)

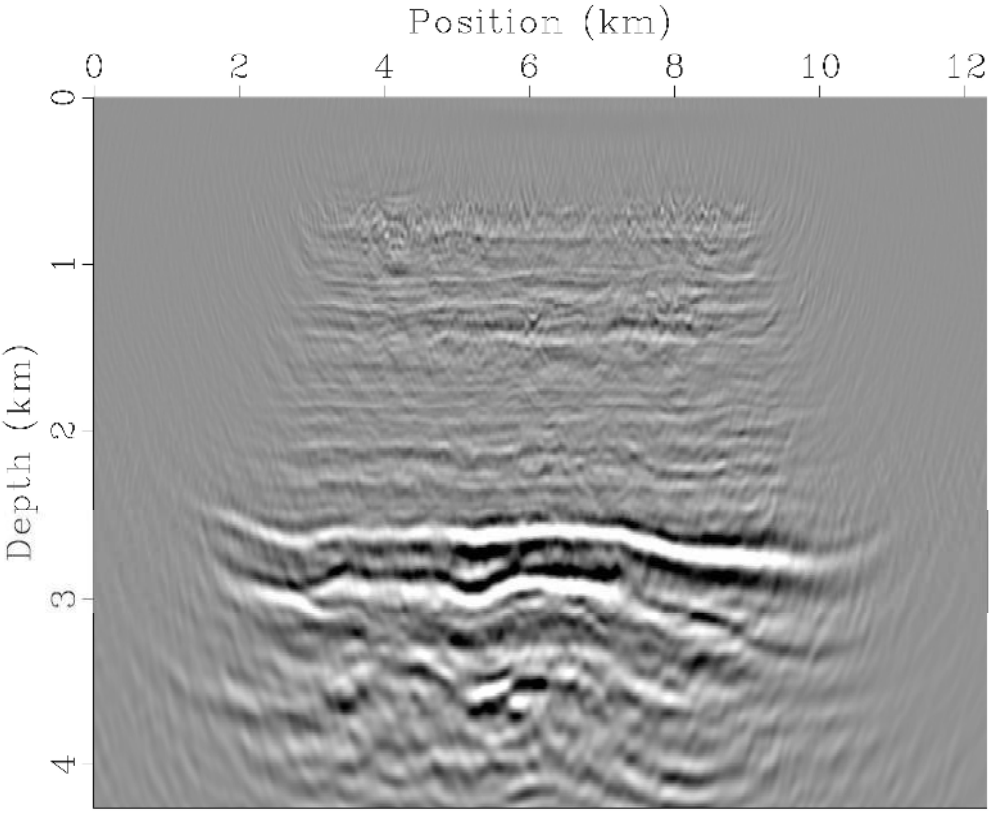

Figure 13 (b)

225x185mm (300 x 300 DPI)

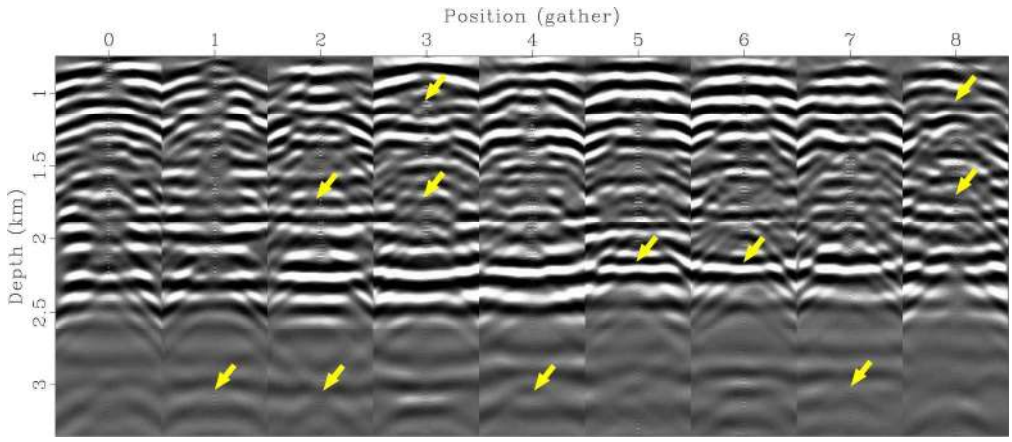

Figure 14 (a)

220x94mm (300 x 300 DPI)

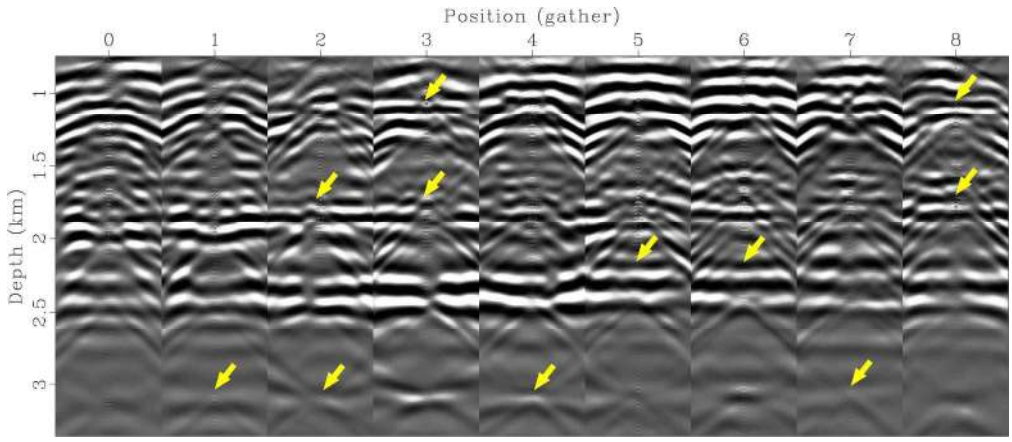

Figure 14 (b)

220x94mm (300 x 300 DPI)